Lithos 140-141 (2012) 183–199

Contents lists available at SciVerse ScienceDirect

Lithos

journal homepage: www.elsevier.com/locate/lithos

Early Jurassic high-K calc-alkaline and shoshonitic rocks from the Tongshi intrusive complex, eastern North China Craton: Implication for crust–mantle interaction and post-collisional magmatism

Ting-Guang Lan [a], Hong-Rui Fan [a,*], M. Santosh [b], Fang-Fang Hu [a], Kui-Feng Yang [a], Yue-Heng Yang [c], Yongsheng Liu [d]

[a] Key Laboratory of Mineral Resources, Institute of Geology and Geophysics, Chinese Academy of Sciences, Beijing 100029, China
[b] Division of Interdisciplinary Science, Faculty of Science, Kochi University, Kochi 780-8520, Japan
[c] State Key Laboratory of Lithospheric Evolution, Institute of Geology and Geophysics, Chinese Academy of Sciences, Beijing 100029, China
[d] State Key Laboratory of Geological Processes and Mineral Resources, China University of Geosciences, Wuhan 430074, China

ARTICLE INFO

Article history:
Received 6 September 2011
Accepted 20 January 2012
Available online 9 February 2012

Keywords:
High-K calc-alkaline series
Shoshonitic series
Crust–mantle interaction
Post-collisional magmatism
North China Craton

ABSTRACT

The Tongshi intrusive complex, located within the western Shandong Province (Luxi Block) in the eastern North China Craton, comprises high-K calc-alkaline series (fine-grained quartz monzonite and porphyritic quartz monzonite) and shoshonitic series (coarse- to fine-grained porphyritic syenites). Here we report comprehensive data on petrology, geochemistry, Sr–Nd–Pb isotopes and zircon U–Pb and Hf isotopic compositions from the intrusive complex. LA–ICPMS zircon U–Pb ages show that this complex was emplaced at 180.1–184.7 Ma. The fine-grained quartz monzonite and porphyritic quartz monzonite have similar major and trace elements features, implying a similar petrogenetic history. Coupled with the widespread Neoarchean inherited zircons in these rocks, the high SiO_2 and Na_2O as well as the low MgO contents and low Pb isotopic ratios ($(^{206}Pb/^{204}Pb)_i = 15.850–16.881$, $(^{207}Pb/^{204}Pb)_i = 14.932–15.261$, $(^{208}Pb/^{204}Pb)_i = 35.564–36.562$) of the quartz monzonites suggest an origin from ancient tonalite–trondhjemite–granodiorite (TTG) crust. However, their higher Nd and Hf isotopic ratios ($\varepsilon_{Nd}(t) = -11.7$ to -7.0, $\varepsilon_{Hf}(t) = -25.0$ to -10.3) as compared to the basement rocks indicate input of enriched lithospheric mantle-derived materials. The coarse- to fine-grained porphyritic syenites were derived from similar sources as inferred from their comparable major and trace elements contents as well as the Nd, Hf and Pb isotopic compositions. The Neoarchean inherited zircons and depletion of Nb, Ta, P and Ti in these rocks indicate the involvement of ancient crust. However, the high Nd and Hf isotopic ratios ($\varepsilon_{Nd}(t) = -0.8$ to 1.5, $\varepsilon_{Hf}(t) = -4.4$ to 4.8) coupled with high Pb isotopic compositions ($(^{206}Pb/^{204}Pb)_i = 18.082–19.560$, $(^{207}Pb/^{204}Pb)_i = 15.510–15.730$, $(^{208}Pb/^{204}Pb)_i = 37.748–39.498$) suggest that the porphyritic syenites were mainly derived from an asthenospheric mantle. Based on the geochemical and isotopic features, a magmatic process similar to MASH (melting, assimilation, storage and homogenization) is proposed for the fine-grained quartz monzonite and AFC (assimilation and fractional crystallization) is envisaged for the porphyritic quartz monzonite and porphyritic syenites. Our data suggest the interaction of various crustal and mantle sources including lower to upper crust, lithospheric mantle and asthenospheric mantle in the generation of the Tongshi intrusive complex. Sharing common characteristics with other post-collisional magmatic rocks, the high-K calc-alkaline and shoshonitic rocks from the Tongshi complex are considered to have originated in post-collisional setting, marking the beginning of lithospheric destruction in the inner domains of the NCC during Mesozoic.

1. Introduction

The Triassic continental collision between North China Craton (NCC) and Yangtze Craton (YC) is one of the major geological events in eastern China, which not only led to the formation of the largest (>30,000 km^2) and best-exposed ultrahigh-pressure (UHP) metamorphic terranes recognized so far on the earth (Ernst et al., 2007; Zheng, 2008), but also reactivated the NCC by influencing the thermal and integral structure of the craton (Xu et al., 2009). Several late Triassic plutons which were emplaced at the southern and eastern margin of the NCC or along the collisional belt have been regarded as the result of post-collisional magmatism (Peng et al., 2008; Seo et al., 2010; Williams et al., 2009; Yang and Wu, 2009; Yang et al., 2007) based on their close spatial and temporal relationship with the collision zone. The various magmatic pulses associated with the post-collisional tectonic regime, and their petrogenetic history

* Corresponding author. Tel.: +86 10 82998218; fax: +86 10 62010846.
E-mail address: fanhr@mail.igcas.ac.cn (H.-R. Fan).

0024-4937/$ – see front matter © 2012 Elsevier B.V. All rights reserved.
doi:10.1016/j.lithos.2012.01.015

indicating intense crust–mantle interaction suggest that at least the eastern margin of the NCC was strongly reactivated and the destruction of the NCC was initiated in the Late Triassic (Yang and Wu, 2009; Yang et al., 2007). However, the effect of the collision in the lithosphere within the inner domain of the NCC is still unclear due to the lack of corresponding magmatic activities.

The Tongshi intrusive complex, an isolated early Jurassic plutonic complex which occurs within the Luxi Block, eastern NCC, provides a key to evaluate the post-collisional magmatism and the initiation of lithospheric reactivation in the inner domains of the NCC. In this study, we report petrological, geochronological, and geochemical data from the Tongshi intrusive complex with a view to constrain its petrogenesis and to evaluate the significance on the lithospheric evolution in eastern NCC.

2. Geological background

The North China Craton, with an Archean core of 2.5–3.8 Ga, is one of the largest and oldest craton in East Asia (Zhai and Santosh, 2011, and references therein). This NCC comprises the Eastern and Western Blocks which amalgamated along the Trans-North China Orogen to form a coherent craton (Fig. 1a), and timing of the assembly is

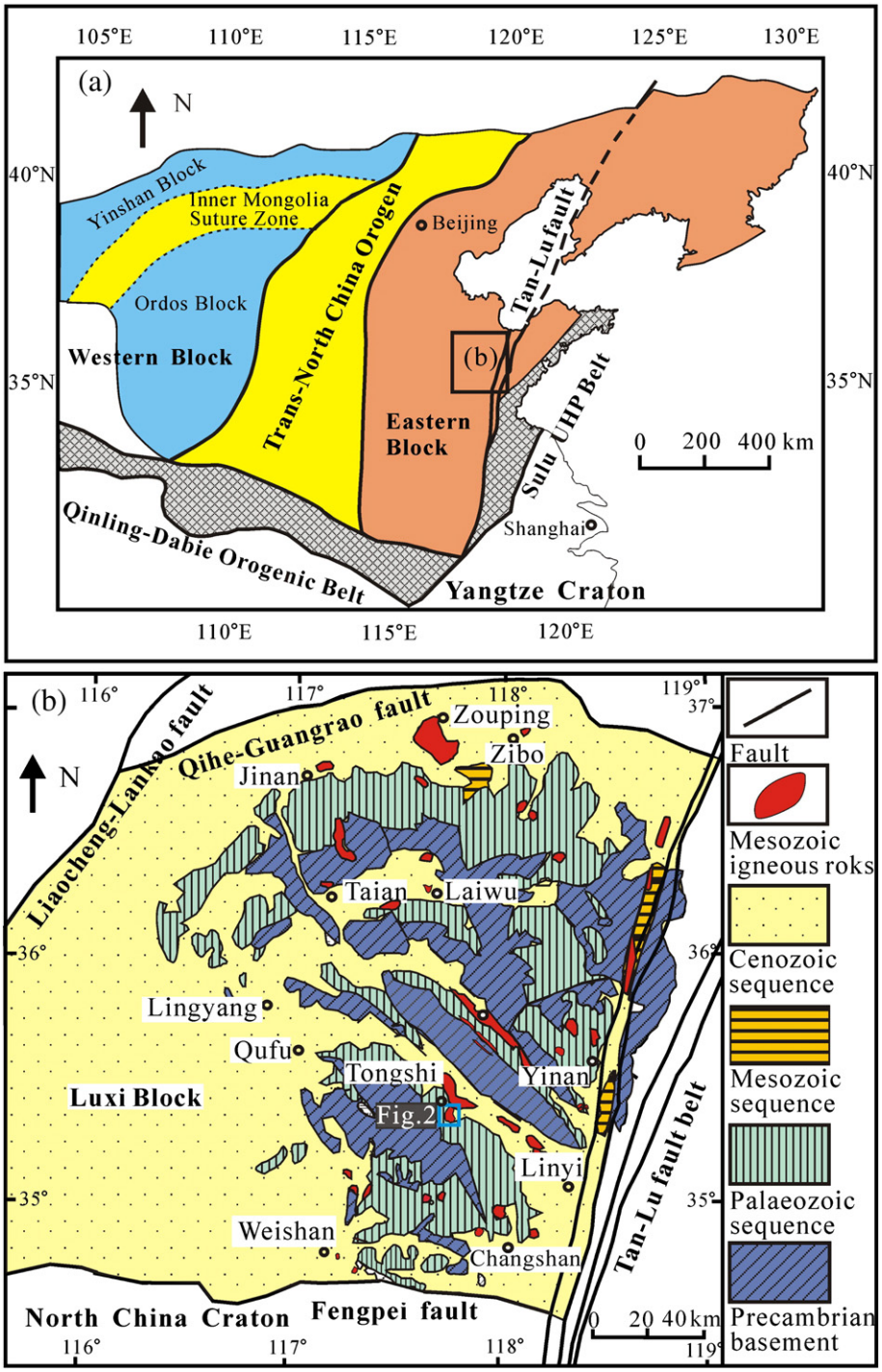

Fig. 1. (a) Geologic and tectonic map of the North China Craton and the location of Luxi Block, modified after Zhao et al. (2005) and Santosh (2010). (b) Geological map of the Luxi Block, modified after Zhang et al. (2007).

considered as at ~1.85 Ga by some workers (Santosh, 2010; Zhao et al., 2001, 2005) whereas others attribute it to Neoarchean (Kusky, 2011). The basement of the NCC consists predominantly of Archean to Paleoproterozoic tonalitic–trondhjemitic–granodioritic (TTG) gneisses and greenschist to granulite facies volcano-sedimentary rocks (Zhao et al., 2001). The cover sequence is predominantly composed of Paleo-Mesoproterozoic to Ordovician volcano-sedimentary rocks, Carboniferous to Permian terrestrial clastic rocks, and Mesozoic basin deposits (Zhang et al., 2005). After its cratonization, the NCC remained largely stable until Mesozoic, prior to the reactivation, large-scale replacement and substantial thinning of the lithosphere (Gao et al., 2002; Griffin et al., 1998; Menzies and Xu, 1998; Zhang et al., 2002, 2011). Since the nature and stability of the sub-continental lithospheric mantle beneath the NCC, particularly towards the eastern part of the craton were substantially modified, several workers have referred to the process as craton destruction (Gao et al., 2009; Wu et al., 2008; Xu et al., 2009; Zhang, 2009).

The Luxi Block is located at the eastern domain of the NCC and is bounded by the Tan–Lu Fault to the east, the Liaocheng–Lankao Fault to the west, the Qihe–Guangrao Fault to the north, and the Fengpei Fault to the south (Zhang et al., 2007) (Fig. 1b). The Tan–Lu Fault, thought to extend deep into the lithospheric mantle (Chen et al., 2008; Zhu et al., 2002), not only transported the eastern section of the Dabie–Sulu UHP metamorphic belt northwards for more than 500 km (Zhu et al., 2003), but also controlled the emplacement of the late Mesozoic intrusions by acting as a conduit for asthenospheric upwelling (Chen et al., 2008; Zhu et al., 2003). The Dabie–Sulu UHP metamorphic belt was built through the continental collision between the NCC and the YC during the Triassic (Li et al., 1993). Neoarchean gneisses, amphibolites and TTGs, Paleoproterozoic granitoids, Paleozoic carbonates interbedded with clastic rocks, Mesozoic and Cenozoic continental clastic rocks, volcaniclastics, intermediate-basic igneous rocks, mafic dykes, carbonatites, and alkaline rocks are the major components in the Luxi Block.

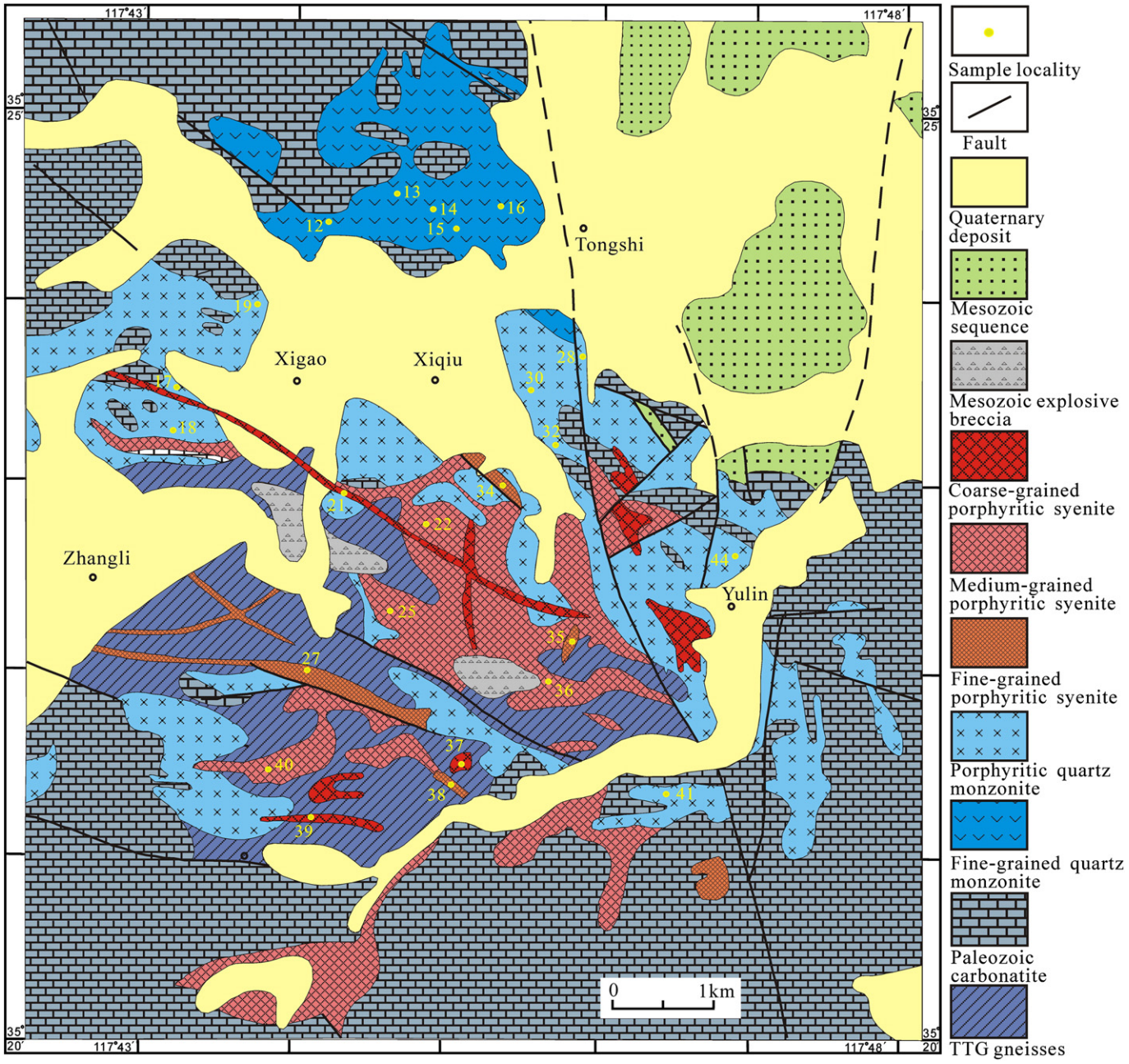

Fig. 2. Geological map of the Tongshi intrusive complex, modified after Geology and Mineral Resources Bureau of Shandong Province (1995).

The 30 km^2 Tongshi intrusive complex intrudes into Neoarchean TTG gneisses as well as Paleozoic carbonates, and consists of fine-grained quartz monzonite, porphyritic quartz monzonite, coarse-grained porphyritic syenite, medium-grained porphyritic syenite and fine-grained porphyritic syenite assemblages (Fig. 2). The fine-grained quartz monzonite, porphyritic quartz monzonite and medium-grained porphyritic syenite constitute the dominant rock types in the complex. Field investigations reveal that the quartz monzonites are intruded by the porphyritic syenites and the medium-grained porphyritic syenite is intruded by the coarse-grained porphyritic syenite. Due to intense weathering and sedimentary cover, the filed relationships of the other rocks are obscure. The complex is mainly distributed in the Tongshi region of Pingyi County, about 100 km west of the Sulu orogenic belt.

3. Petrography

3.1. Fine-grained quartz monzonite

The fine-grained quartz monzonite (Fig. 3a) consists mainly of feldspar and hornblende with subordinate quartz and pyroxene and accessory titanite and ilmenite. The volumetrically dominant (>80 vol.%) feldspar crystals are subhedral–anhedral (0.05–2.8 mm) and characterized by the intergrowth of plagioclase and orthoclase. The plagioclase crystals are mainly andesine to labradorite. The euhedral–anhedral hornblende grains (0.2–1.5 mm) are tschermakite and Magnesiohastingsite (~15 vol.%). The scattered anhedral quartz grains (<5 vol.%) are 0.05–0.1 mm in size. The rare anhedral pyroxene crystals (<0.3 mm) are compositionally diopside.

3.2. Porphyritic quartz monzonite

The porphyritic quartz monzonite (Fig. 3b) dominantly comprises feldspar and hornblende, with subordinate quartz and accessory titanite, monazite and magnetite. The feldspar can be divided into phenocryst and matrix phases based on grain size. The euhedral–subhedral feldspar phenocrysts (>65 vol.%) are mainly andesine (0.5–4.5 mm). The anhedral matrix feldspars (20 vol.%) are intergrown orthoclase and albite (0.05–0.2 mm). The granular to prismatic hornblende crystals (10 vol.%) are hastingsite (0.05–0.2 mm). The scattered anhedral quartz grains (<5 vol.%) are about 0.5 mm in size.

3.3. Coarse-grained porphyritic syenite

The coarse-grained porphyritic syenite (Fig. 3c) is dominantly composed of alkali–feldspar with accessory magnetite. The feldspar can be divided into three groups according to grain size: coarse, medium, and fine. The coarse feldspar phenocrysts (10 vol.%) are euhedral with lengths varying from 10 mm to 30 mm. The medium-grained feldspar phenocrysts are subhedral–anhedral (30 vol.%) with lengths varying from 0.8 mm to 2 mm. The anhedral fine feldspar crystals (60 vol.%) have bamboo leaf-shaped morphology with lengths less than 0.1 mm.

3.4. Medium-grained porphyritic syenite

The medium-grained porphyritic syenite (Fig. 3d) contains dominantly alkali–feldspar. The feldspar crystals can be divided into phenocryst and matrix phases according to size. The euhedral–subhedral feldspar phenocrysts (25 vol.%) are albite, analbite and orthoclase with lengths varying from 0.5 mm to 5 mm. The anhedral matrix feldspars (85 vol.%) are mainly intergrown orthoclase and albite (~0.05 mm).

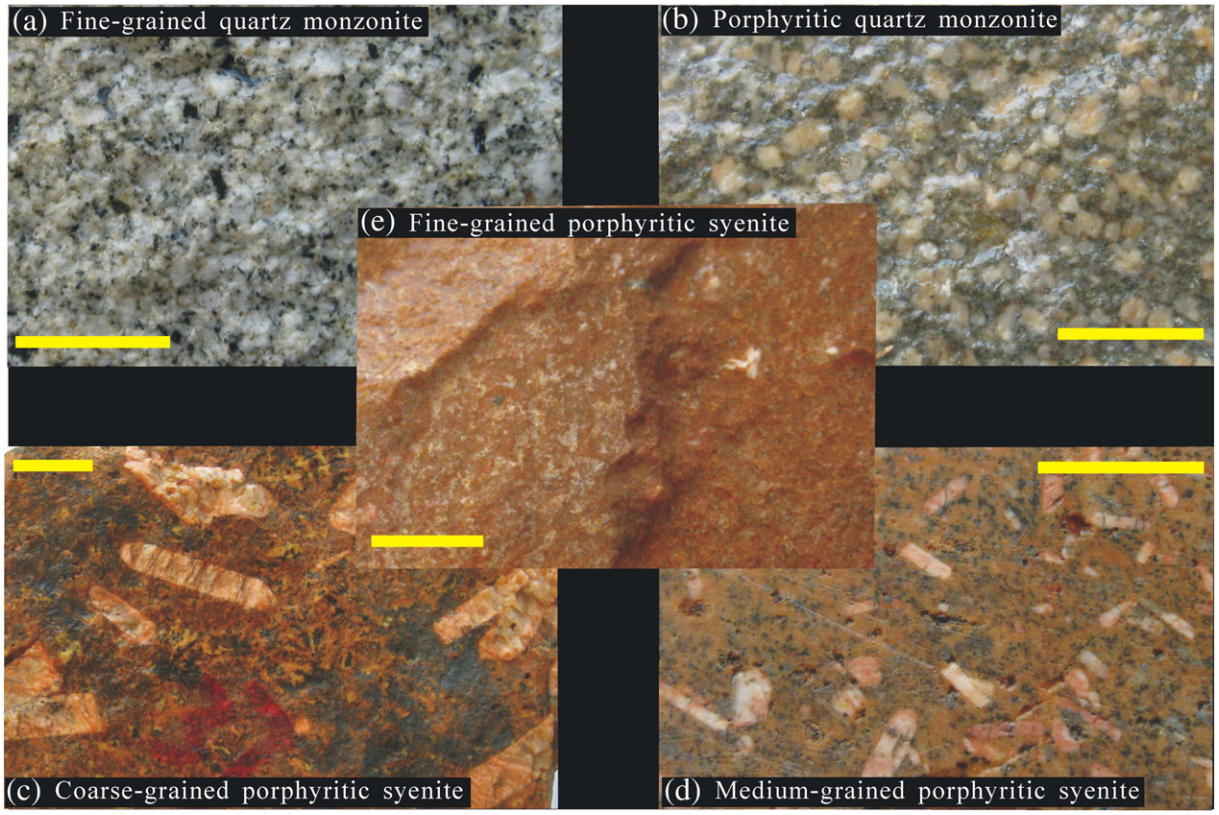

Fig. 3. Representative petrographic pictures of fine-grained quartz monzonite (a), porphyritic quartz monzonite (b), coarse-grained porphyritic syenite (c), medium-grained porphyritic syenite (d) and fine-grained porphyritic syenite (e) from the Tongshi intrusive complex. The scale bar is 1 cm in the picture.

3.5. Fine-grained porphyritic syenite

The fine-grained porphyritic syenite (Fig. 3e) consists dominantly of orthoclase with accessory magnetite. The orthoclase grains can be divided into phenocryst and matrix phases. The subhedral–anhedral feldspar phenocrysts (10 vol.%) are granular or columnar with lengths varying from 0.8 mm to 4 mm. The anhedral matrix feldspars (90 vol.%) are columnar or irregular with lengths less than 0.5 mm. The scattered magnetite grains are granular and smaller than 0.15 mm.

4. Analytical methods

Fresh rock samples were selected for petrography from thin sections, 200 mesh powder for major, trace elements, and Sr–Nd–Pb isotope analyses, and 40–60 mesh crushings for separating zircon grains for U–Pb dating and Hf analyses.

4.1. Mineral compositions and cathodoluminescence (CL) images of zircon grains

Mineral compositions and CL images of zircon grains were obtained using a CAMECA SX50 electron microprobe at the Institute of Geology and Geophysics, Chinese Academy of Sciences (IGGCAS). The operating conditions were 15 kV accelerating voltage and 20 nA beam current.

4.2. Major and trace elements

Major and trace elements were analyzed in the Major and Trace Elements Laboratories of IGGCAS. For major element analyses, mixtures of whole rock powders (0.5 g) and $Li_2B_4O_7 + LiBO_2$ (5 g) were made into glass disks and analyzed by X-ray fluorescence spectroscopy (XRF) with an AXIOS Minerals spectrometer. The analytical uncertainties were generally within 0.1–1% (RSD). For trace element analyses, whole rock powders (40 mg) were dissolved in distilled $HF + HNO_3$ in Teflon screw-cap capsules at 200 °C for 5 days, dried, and then digested with HNO_3 at 150 °C for 1 day. The final step was repeated once. Dissolved samples were diluted to 49 ml with 1% HNO_3 and 1 ml 500 ppb indium was added to the solution as an internal standard. Trace element abundances were determined by inductively coupled plasma mass spectrometry (ICPMS) using a Finnigan MAT Element spectrometer. A blank solution was prepared and the total procedural blank was <100 ng for all trace elements. Multi-element standard solution was measured for matrix effects and instrument drift correction. Precision for all trace elements is estimated to be 5% and accuracy is better than 5% for most of the elements as evaluated from the GSR1 standard.

4.3. Sr, Nd and Pb isotopes

Whole rock powders for Sr and Nd isotopic analyses were dissolved in Teflon bombs after being spiked with ^{87}Rb, ^{84}Sr, ^{149}Sm and ^{150}Nd tracers prior to $HF + HNO_3 + HClO_4$ dissolution. Rb, Sr, Sm and Nd were separated using conventional ion exchange procedures and measured using a Finnigan MAT262 multi-collector mass spectrometer at IGGCAS. Procedural blanks are <100 pg for Sm and Nd and <300 pg for Rb and Sr. The isotopic ratios were corrected for mass fractionation by normalizing to $^{86}Sr/^{88}Sr = 0.1194$ and $^{146}Nd/^{144}Nd = 0.7219$, respectively. The measured values for the JNdi-1 Nd standard and NBS987 Sr standard were $^{143}Nd/^{144}Nd = 0.512118 \pm 12$ (2σ, n = 10) and $^{87}Sr/^{86}Sr = 0.710257 \pm 12$ (2σ, n = 10), respectively. USGS reference material BCR-2 was measured to monitor the accuracy of the analytical procedures, with the following results: $^{143}Nd/^{144}Nd = 0.512633 \pm 13$ (2σ, n = 12) and $^{87}Sr/^{86}Sr = 0.705035 \pm 12$ (2σ, n = 12).

For Pb isotope determination, the whole rock powders were dissolved in Teflon vials with purified $HF + HNO_3$ at 120 °C for 7 days and then separated using anion-exchange columns with diluted HBr as elutant. Isotopic ratios were also measured by the Finnigan MAT262 multi-collector mass spectrometer in IGGCAS. Repeated analyses of Pb isotope standard NBS981 yielded $^{206}Pb/^{204}Pb = 16.890 \pm 0.013$, $^{207}Pb/^{204}Pb = 15.426 \pm 0.014$ and $^{208}Pb/^{204}Pb = 36.514 \pm 0.014$. Relative to the following values for NBS981: $^{206}Pb/^{204}Pb = 16.941$, $^{207}Pb/^{204}Pb = 15.496$ and $^{208}Pb/^{204}Pb = 36.722$ (Galer and Abouchami, 1998), Pb isotopic data in samples were corrected for mass fractionation of 0.15% per atomic mass unit for $^{206}Pb/^{204}Pb$, $^{207}Pb/^{204}Pb$ and $^{208}Pb/^{204}Pb$.

4.4. Zircon U–Pb dating and in situ Hf isotopic analyses

U–Pb dating and trace element analyses of zircon were conducted synchronously by LA–ICPMS at the State Key Laboratory of Geological Processes and Mineral Resources, China University of Geosciences, Wuhan. Detailed operating conditions for the laser ablation system and the ICPMS instrument and data reduction are similar to those described by Liu et al. (2008, 2010). Laser sampling was performed using a GeoLas 2005 coupled with an Agilent 7500a ICPMS instrument. A laser spot size of 32 μm and a laser repetition of 6 Hz were used during the analyses. Quantitative calibration for trace element analyses and U–Pb dating were performed by *ICPMSDataCal* (Liu et al., 2008, 2010). Zircon 91500 was used as external standard for U–Pb dating, and was analyzed twice every 5 analyses. Concordia diagrams and weighted mean calculations were made using Isoplot/Ex_ver 3 (Ludwig, 2003).

In-situ zircon Hf isotopic analyses were conducted on the same spots which were analyzed for U–Pb dating. Hf isotopic compositions were determined by a Neptune MC–ICPMS equipped with a GeolasPlus 193 nm ArF excimer laser at the IGGCAS. Laser spot size of 40 μm and laser repetition of 8 Hz with energy density of 15 J/cm^2 were used during the analyses. The signal collection model is one block with 200 cycles, with an integration time of 0.131 s for one cycle and a total time of 26 s during each analysis. Zircon 91500 was used as external standard for Hf isotopic analyses and was analyzed twice every 5 analyses. Replicate analyses of 91500 yielded a mean $^{176}Hf/^{177}Hf$ ratio of 0.282300 ± 24 (2σ) which is concordant with the $^{176}Hf/^{177}Hf$ ratios measured by Goolaerts et al. (2004) and Woodhead et al. (2004). The detailed analytical procedures are described in Xie et al. (2008).

5. Results

5.1. Geochronology

All the rocks except for the coarse-grained porphyritic syenite yielded adequate zircons for LA–ICPMS U–Pb dating.

5.1.1. Fine-grained quartz monzonite

Zircon crystals in the fine-grained quartz monzonite (Sample 08LX15) can be divided into two types. Zircons of the first type are mainly granular and rounded and are white to gray with indistinct oscillatory zoning in CL images; those of the second type are smaller and much less than the first type and are generally dark in CL images (Fig. 4a). Four analyses of the first type yield $^{207}Pb/^{206}Pb$ ages of 2474–2511 Ma, indicating the presence of Neoarchean inherited zircons in the fine-grained quartz monzonite. Fourteen analyses of the second type are concordant and yield a mean $^{206}Pb/^{238}U$ age of 184.7 ± 1.0 Ma (2σ) (Fig. 5a and Appendix Table S1).

5.1.2. Porphyritic quartz monzonite

Zircon crystals in the porphyritic quartz monzonite (Sample 08LX44) range from 100 to 500 μm in size, with length to width ratios

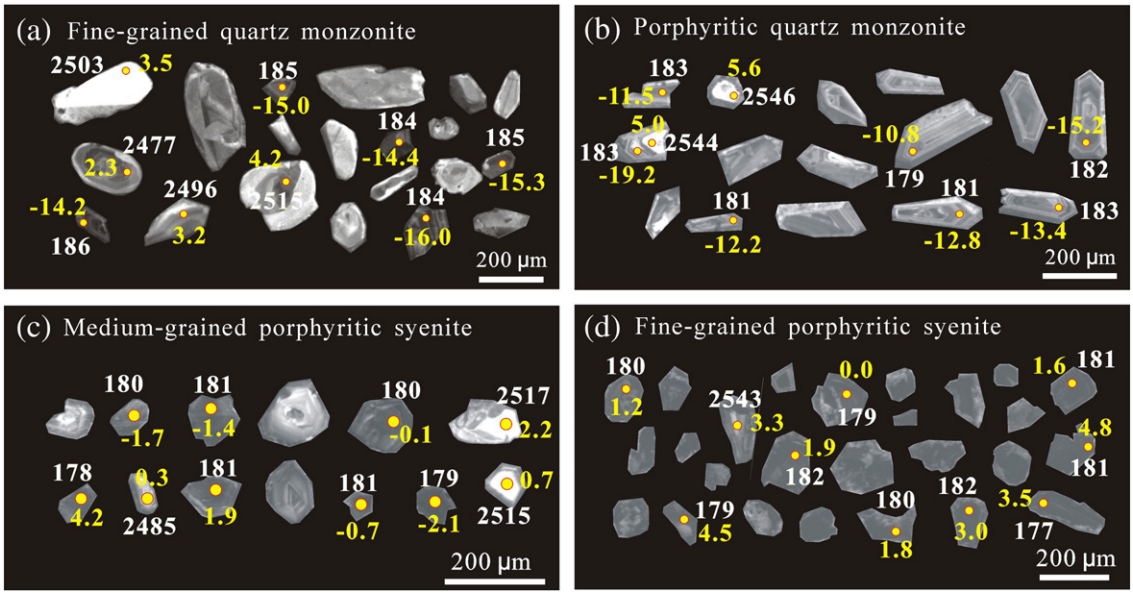

Fig. 4. Representative CL images of zircon grains from the Tongshi intrusive complex. Zircon U–Pb ages (Ma) and $\varepsilon_{Hf}(t)$ values are also shown.

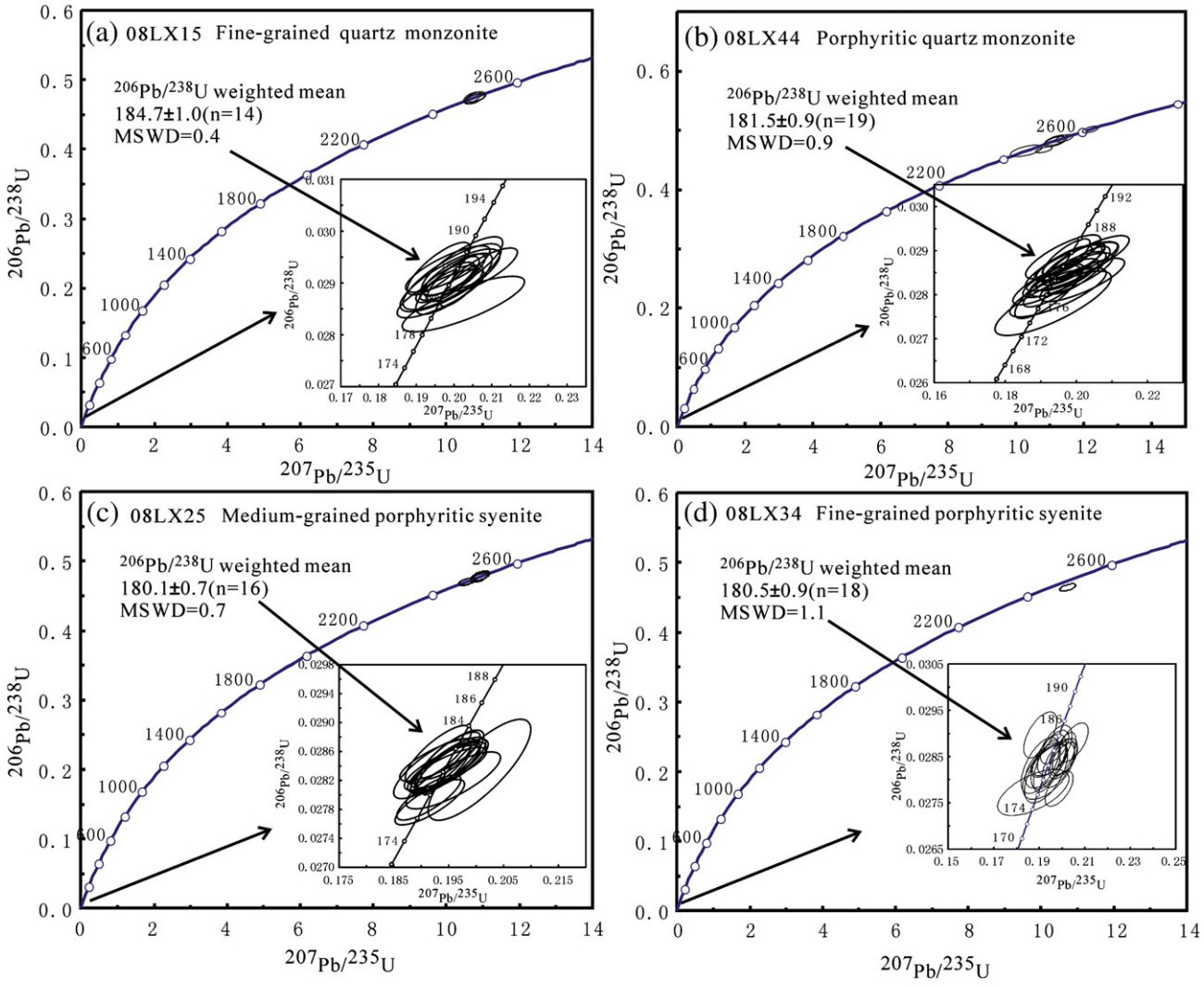

Fig. 5. LA–ICPMS zircon U–Pb concordia diagrams of fine-grained quartz monzonite (a), porphyritic quartz monzonite (b), medium-grained porphyritic syenite (c) and fine-grained porphyritic syenite (d) from the Tongshi intrusive complex.

of 1:1 to 3:1. Most grains are euhedral–subhedral and are gray in CL images with wide oscillatory zoning in the cores and narrow oscillatory zoning in the rims. A few grains have white cores mantled by gray overgrowths (Fig. 4b). The nineteen analyses from CL-dark euhedral–subhedral grains are concordant and yield a mean $^{206}Pb/^{238}U$ age of 181.5 ± 0.9 Ma (2σ) (Fig. 5b and Appendix Table S1). Six analyses conducted on white cores yield $^{207}Pb/^{206}Pb$ ages of 2458–2608 Ma, indicating that Neoarchean to early Proterozoic inherited zircons were also captured in the porphyritic quartz monzonite.

5.1.3. Medium-grained porphyritic syenite

Zircon crystals in the medium-grained porphyritic syenite (Sample 08LX25) are grainy and range from 100 to 350 μm in size. They can be divided into two types: the first type is more or less rounded with white to gray grains showing indistinct oscillatory zoning in CL images. The second type is dark and also displays indistinct oscillatory zoning in CL images. (Fig. 4c). Six analyses of the first type yield $^{207}Pb/^{206}Pb$ ages of 2484–2518 Ma, which are similar to those of the porphyritic quartz monzonite. Sixteen analyses of the second type yield a mean $^{206}Pb/^{238}U$ age of 180.1 ± 0.7 Ma (2σ) (Fig. 5c and Appendix Table S1).

5.1.4. Fine-grained porphyritic syenite

Zircon crystals in the fine-grained porphyritic syenite (Sample 08LX34) are granular and anhedral and have sizes mainly ranging from 100 to 150 μm. Most grains are dark with indistinct oscillatory zoning in CL images (Fig. 4d). Eighteen analyses are concordant and yield a mean $^{206}Pb/^{238}U$ age of 180.5 ± 0.9 Ma (2σ). (Fig. 5d and Appendix Table S1). One gray zircon yields a $^{207}Pb/^{206}Pb$ age of 2543 Ma, indicating that Neoarchean inherited zircons also exist in the fine-grained porphyritic syenite, although these are much less in abundance as compared to those in the other rocks of present study.

5.2. Mineral chemistry

5.2.1. Feldspar

Feldspar is the most abundant mineral in the Tongshi intrusive complex. However, the feldspars in quartz monzonites and porphyritic syenites show contrasting composition. Besides orthoclase, other feldspars are classified into andesine to labradorite ($Ab_{56-71}An_{25-43}Or_{1-4}$) in the fine-grained quartz monzonite and the Ab component increases from the cores to rims in most feldspar crystals. In the porphyritic quartz monzonite, feldspars of phenocrysts can be classified into andesine and matrix feldspars are orthoclase and albite. Only alkali–feldspars occur in the porphyritic syenites, including orthoclase and albite (Appendix Table S2).

5.2.2. Amphibole

Amphibole mainly occurs in the quartz monzonites and is a calcic variety ranging in composition from tschermakite to hastingsite (Appendix Table S3) according to the nomenclature of amphiboles recommended by International Mineralogical Association Commission on New Minerals and Mineral Names (Leake et al., 1997). The porphyritic quartz monzonite contains only hastingsite, whereas the fine-grained quartz monzonite carries both tschermakite and hastingsite.

5.3. Major and trace elements

Major and trace element analyses are presented in Table 1.

5.3.1. Quartz monzonites

The fine-grained quartz monzonite and porphyritic quartz monzonite have similar SiO_2 (62.4–65.8 wt.%), Al_2O_3 (17.0–18.4 wt.%), $Fe_2O_3^t$ (2.7–4.2 wt.%), TiO_2 (0.23–0.38 wt.%), MgO (0.46–0.98 wt.%) and P_2O_5 (0.10–0.18 wt.%) contents, although the CaO (3.8–4.4 wt.%) and $Na_2O + K_2O$ (8.06–8.13 wt.%) contents of the fine-grained quartz monzonite are higher and lower than the CaO (1.7–3.9 wt.%) and $Na_2O + K_2O$ (7.4–9.9 wt.%, average 9.0 wt.%) contents of the porphyritic quartz monzonite. Almost all the samples fall into the field of quartz monzonite in the SiO_2 vs. $Na_2O + K_2O$ classification diagram (Fig. 6a) and are chemically metaluminous (Fig. 6b). The moderate to high $Na_2O + K_2O$ contents of the fine-grained quartz monzonite and the porphyritic quartz monzonite group these rocks in the calc-alkaline and alkaline fields when plotted on the SiO_2–A.R. diagram (Fig. 6c). These rocks belong to high-K calc-alkaline series in the K_2O–SiO_2 diagram (Fig. 6d), although their Na_2O contents are higher than the K_2O contents (Na_2O/K_2O = 1.6–2.3, average 2.0).

The concentrations and distribution patterns of REE and trace elements of the fine-grained quartz monzonite and porphyritic quartz monzonite are nearly identical. All of the rocks are characterized by LREE enrichment, moderate fractionation between LREE and HREE ($(La/Yb)_N$ = 11–14), and slight or no negative Eu anomalies (δEu = 0.86–1.04) (Fig. 7a). On the primitive mantle-normalized spidergrams, they show enrichment in LILEs such as Rb, Sr, Ba and strong depletion in HFSEs such as Nb, Ta, Zr, Hf, P and Ti (Fig. 7b).

5.3.2. Porphyritic syenites

All the samples of the coarse- to fine-grained porphyritic syenites fall in the field of alkali feldspar syenite except for three samples which fall in the field of syenite in the QAP diagram (Fig. 6a). There is no apparent difference in the SiO_2 contents (60.3–62.7 wt.%) between these rocks. However, the TFe_2O_3, MgO and CaO contents systematically decrease from the coarse-grained porphyritic syenite (2.7–4.0 wt.%, 0.14–0.25 wt.%, 0.15–0.62 wt.%) through medium-grained porphyritic syenite (0.9–4.2 wt.%, 0.09–0.63 wt.%, 0.11–0.65 wt.%) to fine-grained porphyritic syenite (0.8–1.4 wt.%, 0.05–0.12 wt.%, 0.03–0.26 wt.%). All the rocks are enriched in Al_2O_3 (18.9–21.6 wt.%) and are thus chemically peraluminous (Fig. 6b). The exceptionally high K_2O contents increase from coarse-grained porphyritic syenite (6.2–14.2 wt.%, average 9.8 wt.%) and medium-grained porphyritic syenite (9.1–11.6 wt.%, average 9.2 wt.%) to fine-grained porphyritic syenite (11.1–15.0 wt.%, average 13.2 wt.%), and classify the rocks as alkaline to peralkaline rock in the SiO_2–A.R. diagram (Fig. 6c) and as shoshonitic series in the K_2O–SiO_2 diagram (Fig. 6d). The relatively low Na_2O contents (Na_2O/K_2O = 0.03–0.99) of the porphyritic syenites are obviously different from those of the quartz monzonites.

The porphyritic syenites show similar distribution patterns of REE and trace elements, although the concentrations of REE and trace elements display certain variation. The total contents of REEs systematically decrease from coarse-grained porphyritic syenite ($\sum$REE = 181–307 ppm, average 247 ppm), through medium-grained porphyritic syenite ($\sum$REE = 112–244 ppm, average 170 ppm) to fine-grained porphyritic syenite ($\sum$REE = 33–113 ppm, average 80 ppm). All the rocks are characterized by LREE enrichment ($\sum$LREE = 207–1107 ppm), moderate to strong fractionation between LREE and HREE ($(La/Yb)_N$ = 11–73), and slight or no negative Eu anomalies (δEu = 0.58–0.96) (Fig. 7c). On the primitive mantle-normalized spidergrams, they are enriched in Rb (274–1057 ppm) and strongly depleted in HFSEs (Nb, Ta, P and Ti) and Ba (Fig. 7d). However, no negative Zr and Hf anomalies are observed. The coarse-grained porphyritic syenite and medium-grained porphyritic syenite are slightly enriched in Sr (325–958 ppm), whereas the fine-grained porphyritic syenite is depleted in Sr (46–224 ppm) with the exception of one sample.

5.4. Sr–Nd–Pb–Hf isotopes

Sr, Nd and Pb isotopic compositions of the Tongshi intrusive complex are presented in Table 2 and shown in Figs. 8 and 9. In situ Hf isotopic analyses are shown in Fig. 10 and listed in Appendix Table S4.

Table 1
Major oxides (wt.%) and trace elements (ppm) for the Tongshi intrusive complex.

Rock type	Fine-grained quartz monzodiorite					Porphyritic quartz monzodiorite							
Sample	08LX12	08LX13	08LX14	08LX15	08LX16	08LX17	08LX18	08LX19	08LX28	08LX30	08LX32	08LX41	08LX44
SiO_2	62.8	64.1	63.4	63.3	63.5	65.6	65.8	62.4	63.6	62.7	63.0	64.2	62.6
TiO_2	0.33	0.30	0.32	0.33	0.38	0.23	0.25	0.33	0.30	0.28	0.27	0.29	0.38
Al_2O_3	18.0	17.8	17.8	18.0	17.5	17.8	17.7	17.6	17.4	17.0	17.1	17.6	18.4
TFe_2O_3	4.02	3.78	3.98	3.93	4.16	2.74	2.74	3.80	3.33	3.18	3.12	3.35	4.19
MnO	0.09	0.08	0.12	0.08	0.09	0.10	0.12	0.15	0.11	0.11	0.11	0.12	0.14
MgO	0.90	0.75	0.78	0.77	0.97	0.48	0.46	0.72	0.64	0.68	0.61	0.71	0.98
CaO	4.36	4.15	3.77	3.82	3.87	1.74	2.06	3.89	2.95	3.26	3.94	2.91	2.46
Na_2O	5.59	5.46	5.54	5.49	5.61	6.35	6.01	5.49	6.08	6.03	4.62	6.23	6.28
K_2O	2.48	2.63	2.58	2.64	2.44	2.93	3.19	2.97	3.75	2.67	2.81	2.70	3.62
P_2O_5	0.14	0.15	0.14	0.14	0.17	0.10	0.11	0.15	0.13	0.12	0.11	0.12	0.18
LOI	0.92	0.94	1.56	0.90	1.20	1.50	1.48	2.56	1.70	3.46	4.42	1.82	1.08
Total	99.7	100.1	100.0	99.4	99.9	99.6	99.9	100.0	100.0	99.5	100.1	100.0	100.3
Mg#	30.7	28.2	27.9	28.0	31.6	25.7	24.9	27.3	27.6	29.7	27.9	29.5	31.7
A/NK	1.52	1.51	1.49	1.51	1.48	1.31	1.32	1.43	1.24	1.33	1.60	1.33	1.29
A/CNK	0.91	0.92	0.95	0.95	0.93	1.06	1.03	0.91	0.90	0.91	0.96	0.95	0.98
Sc	4.76	3.79	4.43	4.30	5.51	2.78	2.62	4.12	3.83	3.37	3.29	3.90	4.95
V	41.6	34.9	37.7	38.4	44.4	31.2	32.7	52.0	46.8	32.5	31.7	36.5	59.9
Cr	500	87.2	102	104	121	45.9	55.1	75.5	63.0	68.1	81.8	94.0	44.6
Co	8.74	5.38	5.60	5.74	6.26	1.71	2.59	5.23	4.11	4.32	3.70	4.68	4.96
Ni	246	7.67	5.17	6.95	6.80	3.01	2.20	3.36	2.49	3.81	3.15	4.36	1.56
Cu	28.0	17.4	15.6	17.2	11.0	1.53	1.69	4.01	0.97	1.70	4.32	3.67	3.17
Zn	165	46.4	67.1	48.6	45.8	34.0	49.1	63.7	59.6	49.1	41.0	61.4	64.3
Ga	22.7	22.2	23.2	23.6	22.4	22.9	22.5	23.0	22.4	21.5	21.1	21.4	22.5
Rb	62.3	67.4	76.8	73.4	61.0	89.9	97.1	85.8	112	82.2	99.8	69.0	113
Sr	1271	1264	1339	1267	1040	1371	1184	1387	1093	764	852	1410	1378
Cs	1.84	1.97	2.56	1.73	1.95	2.99	4.01	4.11	1.87	3.52	3.26	3.47	3.58
Ba	1104	1177	1248	1158	1050	1076	1120	905	916	1395	746	958	818
Zr	181	143	146	150	160	179	152	141	175	146	146	156	158
Hf	4.41	3.66	3.80	3.84	4.19	4.66	4.10	3.87	4.77	3.95	3.84	4.21	4.28
Nb	7.22	7.07	7.37	7.34	6.97	7.20	7.06	7.39	7.38	7.50	7.18	7.14	7.27
Ta	0.35	0.36	0.36	0.38	0.34	0.36	0.38	0.38	0.37	0.40	0.37	0.40	0.37
La	39.1	34.7	43.7	41.7	37.6	31.1	30.5	41.4	43.1	31.3	31.3	33.9	42.6
Ce	83.1	74.0	85.7	85.9	79.3	64.4	61.6	87.4	88.4	64.0	61.8	67.9	85.7
Pr	10.7	9.5	11.4	11.1	9.83	8.0	7.9	10.8	10.7	8.30	8.25	8.61	10.9
Nd	41.1	37.9	44.8	43.7	36.3	29.5	31.2	43.1	42.0	33.4	31.8	32.4	42.7
Sm	7.87	6.91	7.61	7.57	6.52	5.59	5.85	7.62	7.24	5.80	5.83	5.70	7.56
Eu	1.97	1.79	2.03	2.00	1.84	1.53	1.57	2.14	1.91	1.63	1.71	1.76	2.26
Gd	5.70	5.25	6.16	6.28	5.03	4.31	4.36	5.71	5.23	4.76	4.64	4.40	6.19
Tb	0.74	0.67	0.78	0.78	0.64	0.59	0.61	0.76	0.71	0.63	0.60	0.61	0.82
Dy	3.77	3.53	4.22	4.03	3.39	3.25	3.40	4.09	3.70	3.36	3.21	3.23	4.47
Ho	0.73	0.68	0.79	0.76	0.66	0.62	0.67	0.82	0.73	0.65	0.63	0.65	0.85
Er	1.99	1.90	2.15	2.10	1.80	1.75	1.83	2.33	2.05	1.76	1.67	1.68	2.36
Tm	0.29	0.28	0.32	0.31	0.27	0.27	0.29	0.37	0.31	0.28	0.25	0.27	0.34
Yb	1.91	1.86	2.14	2.06	1.76	1.75	1.88	2.53	2.18	1.80	1.62	1.72	2.19
Lu	0.29	0.29	0.33	0.32	0.28	0.28	0.29	0.42	0.35	0.27	0.25	0.27	0.32
Y	19.5	18.0	21.9	19.9	18.3	17.4	18.7	22.1	19.6	16.8	16.5	17.1	22.6
Pb	6.19	7.94	7.59	12.5	7.57	8.40	10.31	9.35	5.32	6.93	7.12	9.30	7.85
Th	6.34	5.89	6.58	6.94	5.98	9.01	7.74	11.5	13.0	6.2	6.1	6.8	10.9
U	1.49	1.46	1.66	1.64	1.42	2.84	2.85	3.20	3.47	1.99	1.96	2.13	2.92
δEu	0.86	0.87	0.88	0.86	0.95	0.92	0.91	0.95	0.91	0.92	0.98	1.04	0.98
$(La/Yb)_N$	13.8	12.6	13.8	13.6	14.4	12.0	10.9	11.0	13.3	11.7	13.1	13.3	13.1
T_{Zr} (°C)	762	746	751	754	756	785	769	743	759	747	756	758	759

Rock type	Coarse-grained porphyritic syenite			Medium-grained porphyritic syenite				Fine-grained porphyritic syenite				GSR1	GSR1
Sample	08LX21	08LX37	08LX39	08LX22	08LX25	08LX36	08LX40	08LX27	08LX34	08LX35	08LX38	Avg.	Refer.
SiO_2	61.2	60.6	60.8	60.3	61.0	63.8	63.0	62.3	61.4	62.7	61.9	73.1	72.8
TiO_2	0.48	0.30	0.26	0.20	0.42	0.13	0.12	0.12	0.08	0.12	0.08	0.28	0.28
Al_2O_3	19.2	20.3	19.0	21.6	18.9	20.1	20.1	20.0	19.9	19.6	20.6	13.4	13.4
TFe_2O_3	4.02	2.84	2.65	1.21	4.20	1.77	0.92	0.97	1.20	1.37	0.83	2.13	2.14
MnO	0.15	0.11	0.10	0.01	0.10	0.12	0.03	0.01	0.03	0.04	0.01	0.06	0.06
MgO	0.15	0.25	0.14	0.34	0.63	0.09	0.13	0.12	0.10	0.05	0.06	0.41	0.42
CaO	0.62	0.27	0.15	0.21	0.65	0.18	0.11	0.07	0.08	0.26	0.03	1.54	1.55
Na_2O	6.15	4.05	0.68	2.14	5.84	6.34	2.64	2.25	0.68	3.57	0.43	3.11	3.13
K_2O	6.22	9.12	14.2	11.6	6.92	7.00	11.5	12.0	14.8	11.1	15.0	5.02	5.01
P_2O_5	0.28	0.11	0.09	0.07	0.18	0.03	0.03	0.03	0.02	0.10	0.02	0.09	0.09
LOI	1.60	1.70	1.42	2.16	1.22	1.02	1.28	1.48	1.22	1.00	1.06	0.69	0.69
Total	100.1	99.7	99.4	99.8	100.1	100.7	99.8	99.3	99.5	99.9	100.0	99.8	99.6
Mg#	6.9	14.8	9.5	35.7	22.9	9.1	21.9	19.6	14.2	6.8	12.6		
A/NK	1.14	1.23	1.15	1.34	1.11	1.12	1.20	1.20	1.16	1.09	1.21		
A/CNK	1.07	1.19	1.13	1.31	1.04	1.10	1.19	1.19	1.15	1.07	1.21		
Sc	5.80	3.38	3.44	2.64	6.22	1.71	1.31	1.92	1.26	0.79	1.22	6.38	6.1

Table 1 (*continued*)

Rock type	Fine-grained quartz monzodiorite					Porphyritic quartz monzodiorite							
Sample	08LX12	08LX13	08LX14	08LX15	08LX16	08LX17	08LX18	08LX19	08LX28	08LX30	08LX32	08LX41	08LX44
V	106	78.3	560	117	122	96.9	36.0	152	304	55.8	39.0	24.0	24
Cr	32.6	24.2	38.5	12.6	26.4	24.0	35.3	30.1	29.1	24.3	29.5	2.79	5
Co	7.19	3.34	5.76	1.25	5.62	1.43	1.12	0.65	0.68	1.60	0.58	3.40	3.4
Ni	4.54	1.38	2.71	1.44	1.81	0.17	1.59	0.27	3.74	0.19	0.60	3.10	2.3
Cu	10.1	19.3	29.9	4.94	26.8	24.8	5.03	6.74	14.5	54.8	10.1	2.38	3.2
Zn	63.6	75.1	87.2	50.6	87.4	69.8	58.9	15.2	52.8	61.0	22.0	27.9	28
Ga	29.5	27.7	31.5	35.1	31.2	31.1	29.8	28.4	31.9	22.6	30.4	21.0	19
Rb	274	447	948	651	395	346	662	622	928	417	1057	481	466
Sr	751	379	354	538	958	370	325	224	108	1071	45.6	112	106
Cs	4.74	3.11	9.09	4.92	10.9	2.33	3.39	2.46	2.47	2.60	3.66	39.3	38.4
Ba	768	397	468	392	722	423	372	260	231	557	61	337	343
Zr	220	204	359	234	245	278	282	335	427	112	379	170	167
Hf	5.90	5.47	9.67	5.70	7.19	7.44	7.34	8.03	10.48	2.75	9.06	6.50	6.3
Nb	12.9	8.80	10.1	7.37	12.0	6.78	6.83	13.2	11.2	7.39	12.5	41.7	40
Ta	0.69	0.49	0.41	0.37	0.54	0.29	0.32	0.55	0.44	0.45	0.54	7.40	7.2
La	57.9	44.8	32.9	34.0	38.5	25.2	20.0	29.2	12.7	21.4	4.7	53.6	54
Ce	121	110	73.6	72.8	116	52.7	49.8	52.8	29.6	47.9	13.9	108	108
Pr	14.2	10.8	9.22	8.35	9.37	6.21	4.59	5.33	3.65	5.70	2.17	13.3	12.7
Nd	55.1	38.5	34.0	31.4	36.5	23.3	16.5	16.0	12.5	20.5	8.5	48.9	47
Sm	9.86	6.77	5.93	5.62	6.78	4.17	3.31	2.33	1.66	3.17	1.38	10.1	9.7
Eu	2.50	1.71	1.44	1.31	1.70	1.09	0.85	0.47	0.35	0.84	0.20	0.85	0.85
Gd	7.37	5.54	4.63	4.13	5.02	3.36	2.55	1.64	1.14	2.01	0.59	9.36	9.3
Tb	0.92	0.72	0.55	0.70	0.73	0.42	0.32	0.15	0.12	0.19	0.06	1.65	1.65
Dy	4.86	4.05	2.69	4.19	3.86	2.18	1.59	0.63	0.52	0.78	0.23	10.7	10.2
Ho	0.94	0.82	0.48	0.85	0.76	0.40	0.30	0.11	0.09	0.13	0.04	2.25	2.05
Er	2.56	2.31	1.21	2.25	2.14	1.14	0.84	0.29	0.22	0.31	0.08	6.97	6.5
Tm	0.37	0.36	0.16	0.33	0.33	0.17	0.13	0.04	0.03	0.04	0.01	1.12	1.06
Yb	2.49	2.32	1.03	2.16	2.13	1.17	0.87	0.27	0.18	0.24	0.06	7.81	7.4
Lu	0.38	0.37	0.16	0.33	0.34	0.19	0.14	0.04	0.03	0.04	0.01	1.25	1.15
Y	26.8	22.5	12.9	23.8	20.1	12.7	9.9	3.7	3.1	4.3	1.5	63.6	62
Pb	24.6	17.7	456.5	12.7	20.1	200	10.9	40.5	19.4	33.8	33.0	32.8	31
Th	25.1	32.5	47.1	30.2	38.6	35.8	34.6	50.6	37.5	22.7	27.5	55.8	54
U	6.42	7.21	34.0	7.38	12.3	19.9	15.4	8.12	21.8	4.99	21.6	18.9	18.8
δEu	0.86	0.83	0.81	0.79	0.86	0.86	0.86	0.7	0.73	0.96	0.58		
$(La/Yb)_N$	15.7	13.0	21.6	10.6	12.2	14.5	15.5	73.0	47.2	59.5	55.6		
T_{Zr} (°C)	795	801	851	824	800	822	835	851	870	741	864		

LOI: loss on ignition. $Mg^{\#} = 100 \times Mg/(Mg + \sum Fe)$ atomic ratio. T_{Zr} (°C) = 12,900/[2.95 (0.85 *M*) + ln (496,000/Zr_{melt})], *M* = (Na + K + 2Ca)/(Al × Si) cation ratio (Watson and Harrison, 1983). GSR1 is Chinese granite standard. Avg.: average value measured for reference standard. Refer.: recommended value for reference standard.

5.4.1. Quartz monzonites

The initial $^{87}Sr/^{86}Sr$ ratios of the fine-grained quartz monzonite (0.7037–0.7038) and the porphyritic quartz monzonite (0.7037–0.7041) are concordant, whereas the ε_{Nd} (*t*) values and Pb isotopic compositions of the fine-grained quartz monzonite (ε_{Nd} (*t*) = −12.8 to −12.3, $(^{206}Pb/^{204}Pb)_i$ = 15.850–16.184, $(^{207}Pb/^{204}Pb)_i$ = 14.932–15.122, $(^{208}Pb/^{204}Pb)_i$ = 35.564–35.997) are generally lower than those of the porphyritic quartz monzonite (ε_{Nd} (*t*) = −11.7 to −7.0, $(^{206}Pb/^{204}Pb)_i$ = 16.452–16.881, $(^{207}Pb/^{204}Pb)_i$ = 15.113–15.261, $(^{208}Pb/^{204}Pb)_i$ = 35.212–35.562). Zircons from the fine-grained quartz monzonite (08LX15) yield ε_{Hf} (*t*) values between −25.0 and −10.8 with an average value of −16.5, with the exception of the inherited zircons that show positive ε_{Hf} (*t*) values ranging from 2.3 to 4.2. Nineteen analyses obtained from 24 grains for the porphyritic quartz monzonite (08LX44) yield ε_{Hf} (*t*) values between −19.2 and −10.3 with an average value of −12.5. Five analyses obtained from inherited zircons yield positive ε_{Hf} (*t*) values varying from 1.1 to 5.6. The average ε_{Hf} (*t*) value of the fine-grained quartz monzonite is also slightly lower than that of the porphyritic quartz monzonite. It is notable that the ε_{Hf} (*t*) values obtained from the newly grown zircons show wide variations, which could probably reflect contamination from the widespread inherited zircons.

5.4.2. Porphyritic syenites

The initial $^{87}Sr/^{86}Sr$ ratios of the coarse-grained porphyritic syenite (0.702363–0.703767), medium-grained porphyritic syenite (0.7040–0.7049) and fine-grained porphyritic syenite (0.7041–0.7080) vary widely between 0.702363 and 0.708028 with most of them distributed between 0.703685 and 0.704882. In contrast, the ε_{Nd} (*t*) values of the coarse- to fine-grained porphyritic syenite are markedly uniform (ε_{Nd} (*t*) = −0.8 to 1.5). All the samples of the porphyritic syenites show high values of Pb isotopes ($(^{206}Pb/^{204}Pb)_I$ = 18.082–19.560, $(^{207}Pb/^{204}Pb)_i$ = 15.510–15.730, $(^{208}Pb/^{204}Pb)_i$ = 37.748–39.498), which are distinctly different from those of the quartz monzonites. We have no ε_{Hf} (*t*) data for the coarse-grained porphyritic syenite due to the lack of zircons in these rocks. The medium-grained porphyritic syenite and fine-grained porphyritic syenite are characterized by ε_{Hf} (*t*) values of −4.4–4.2 (average −1.0) and 0.0–4.8 (average 2.6). The ε_{Hf} (*t*) values of inherited zircons obtained from these rocks vary from −6.7 to 11.0.

6. Discussion

6.1. Source materials

6.1.1. Quartz monzonites

The similar major and trace elements features, Sr–Nd–Pb–Hf isotopic compositions and close spatial relationship of the fine-grained quartz monzonite and the porphyritic quartz monzonite suggest that these rocks might have originated from similar sources, although they show different intrusive ages and rock textures. These rocks have high SiO_2 (>62.4 wt.%) and low MgO (<0.98 wt.%) contents, suggesting their formation from crust-involved magmas or highly evolved magmas. However, a significant degree of fractionation during magma evolution can be excluded due to the nearly homogeneous major and trace elements concentrations between and within these two types of rocks, especially given the fact that the intrusive age of the porphyritic quartz monzonite is younger than that of the

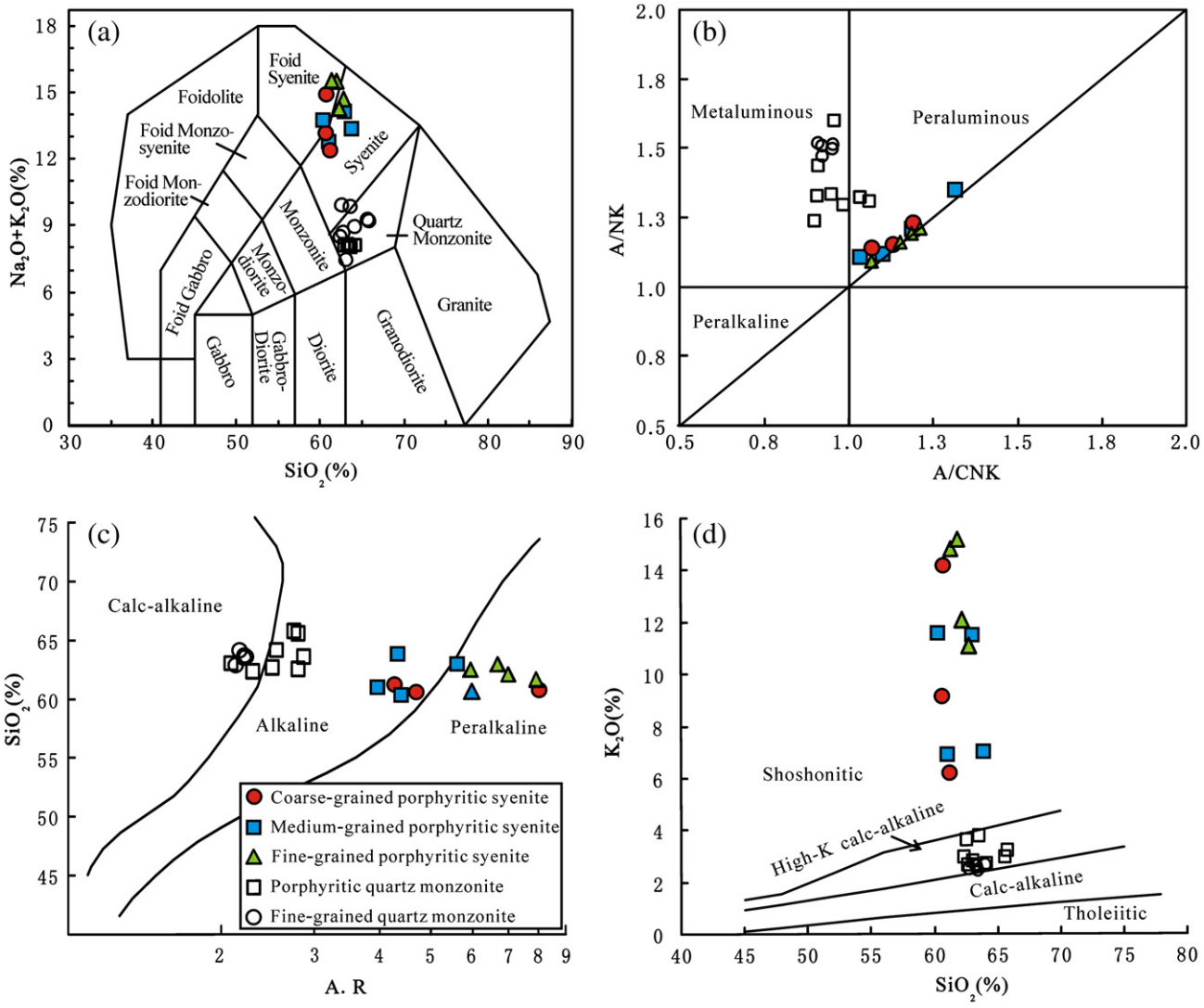

Fig. 6. Plots of SiO_2 vs. Na_2O+K_2O (a), A/NK [molar ratio $Al_2O_3/(Na_2O+K_2O)$] vs. A/CNK [molar ratio $Al_2O_3/(CaO+Na_2O+K_2O)$] (b), SiO_2 vs. A.R [$Al_2O_3+CaO+(Na_2O+K_2O)$]/[$Al_2O_3+CaO-(Na_2O+K_2O)$] (c) and K_2O vs. SiO_2 (d) for the Tongshi intrusive complex.
(a) is from Middlemost (1994), (c) is from Wright (1969) and (d) is from Peccerillo and Taylor (1976).

fine-grained quartz monzonite by about nine million years. The evidently high Na_2O contents ($Na_2O>4.6$ wt.%, $Na_2O/K_2O=1.6$–2.3) of the quartz monzonites, which are similar to those of TTG crust-derived magmas (Nehring et al., 2009; Rapp and Watson, 1995; Watkins et al., 2007), also attribute a genetic link with the surrounding Neoarchean TTG gneisses (Wang, 2010). We therefore infer that the widespread TTG gneisses in the study area might have provided the source materials for the quartz monzonites. The abundant Neoarchean inherited zircons preserved in both the fine-grained quartz monzonite and the porphyritic quartz monzonite are robust indications for the involvement of the Neoarchean crustal materials in the formation of the quartz monzonites. Furthermore, the low Pb isotopic compositions of the quartz monzonites show a trend towards those of the TTG gneisses (Fig. 9), implying the involvement of the Neoarchean crust.

Although the features described above provide a strong case for crustal involvement, the REEs and trace elements features of these rocks, as well as their Nd and Hf isotopic compositions do not lend support to the origin of the quartz monzonites exclusively from crustal sources. The high Sr (764–1410 ppm, average 1202 ppm) and HREEs (Y = 16.5–22.5 ppm, average 19.1 ppm; Yb = 1.6–2.5 ppm, average 2.0 ppm) of the quartz monzonites are far higher than those of the surrounding TTG gneisses (Sr = 118–623 ppm, average 393 ppm; Y = 1.2–23.9 ppm, average 9.8; Yb = 0.1–2.1 ppm, average 0.9 ppm) (Wang, 2010). The quartz monzonites are therefore not products of direct partial melting of the TTGs regardless of melting at shallow or deep crustal levels (Nehring et al., 2009; Zhang et al., 2009). At shallow crustal level ($P\leq 4$ kbar, upper or middle crust), dehydration melting of TTG granitoids (tonalite and granodiorite) is likely to produce A-type granitic melts with strongly negative Eu and Sr anomalies (Patiño Douce, 1997), whereas at deep crustal level (lower crust) garnet granulite would be produced and the partial melting of such granulite would leave the residue rich in Ca-rich plagioclase and garnet, generating magmas with negative Eu anomalies and low HREE contents (Rapp and Watson, 1995; Zhang et al., 2005, 2010). Therefore, other sources enriched in Sr or HREEs are required to account for the features displayed by the quartz monzonites. The Nd isotopic compositions of the quartz monzonites (ε_{Nd} (180 Ma) > −12.8) are much higher than those of the Neoarchean basement rocks (mainly TTGs) of Luxi Block (ε_{Nd} (180 Ma) < −20, Jahn et al., 1988; Wang, 2010), albeit only moderately lower than the nearby mantle-derived Mengyin kimberlites and peridotite xenoliths (Yang et al., 2009; Zhang et al., 2008) (Fig. 8), suggesting that mantle-derived materials also participated in the formation of the quartz monzonites. Furthermore, most of the ε_{Hf} (t) values of the quartz monzonites are higher than those of the lower-crustal xenoliths of

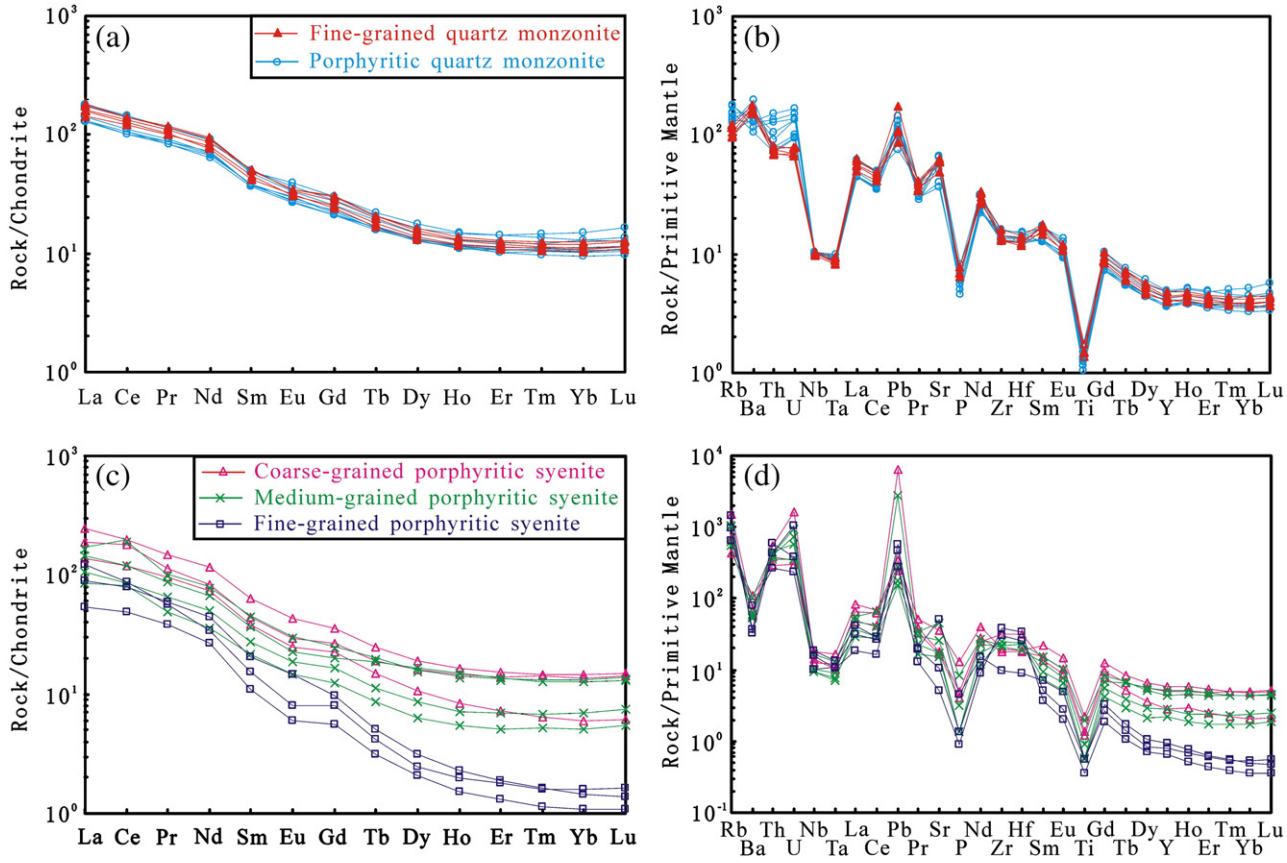

Fig. 7. Chondrite-normalized REE patterns and Primitive Mantle (PM) normalized trace element diagrams for quartz monzonites (a and b) and porphyritic syenites (c and d) from the Tongshi intrusive complex.
Chondrite and PM values are from Sun and McDonough (1989).

NCC (Zheng et al., 2004) and fall above the 2.5 Ga continental crust evolutional line, but are relatively closer to the ε_{Hf} (t) values of the Mengyin kimberlites (Yang et al., 2009) (Fig. 10). Thus, it is reasonable to deduce that mantle-derived materials must be involved in the quartz monzonites. In fact, gabbroic enclaves were found in the quartz monzonites and the presence of such enclaves support the role of mantle-derived melts in the generation of these rocks (Xu et al., 2004). However, the Sr isotopic compositions of the quartz monzonites are lower than those reported for the basement rocks in the study area, making it difficult to quantitatively model the involvement of crust- and mantle-derived materials in magma genesis. Nonetheless, considering the very low MgO contents coupled with absence of any significant fractionation, we infer that the lithospheric mantle probably provided few melts or mainly fluids to elevate the ε_{Nd} (t) and ε_{Hf} (t) values of the quartz monzonites. The presence of more inherited zircons rather than newly grown zircons in the fine-grained quartz monzonite suggests that more crust-derived materials were involved in the formation of the fine-grained quartz monzonite. On the other hand, the average ε_{Nd} (t) and ε_{Hf} (t) values of the fine-grained quartz monzonite are lower than those of the porphyritic quartz monzonite, offering further evidence for more crust-derived materials participating in the formation of the fine-grained quartz monzonite.

6.1.2. Porphyritic syenites

The Neoarchean inherited zircons preserved in the porphyritic syenites indicate that Neoarchean crustal materials must have participated in the formation of the porphyritic syenites. Their high SiO_2 (>60.3 wt.%) and low MgO (<0.63 wt.%) contents as well as Nb, Ta, P and Ti depletion also suggest crustal involvement. However, the whole rock ε_{Nd} (t) values of the porphyritic syenites are much higher than the crust, precluding an exclusive crustal origin. The lithospheric mantle beneath the Luxi Block, as imaged from the Mengyin kimberlites and peridotite xenoliths, do not seem to have contributed significantly as indicated by their lower ε_{Nd} (t) values than those of the porphyritic syenites (Fig. 8). Most of the whole rock ε_{Nd} (t) values and zircon ε_{Hf} (t) values (up to 4.8) of the porphyritic syenites are positive, suggesting their origin from an asthenospheric mantle. In addition, their high Pb isotopic compositions are similar to those of MORB or OIB (Fig. 9). Therefore, combined with the presence of Neoarchean inherited zircons, and the Nd, Hf and Pb isotopic compositions, we infer that the porphyritic syenites mainly originated from the asthenospheric mantle but were contaminated by Neoarchean crustal materials. Notably, the wide ranges of $(La/Yb)_N$ (11–73) ratios as well as Y (0.05–2.49 ppm) and Yb (1.50–26.8 ppm) contents of the porphyritic syenites (Table 1 and Fig. 7) suggest that the crustal materials involved were possibly derived from different depths in the lower crust to middle or upper crust.

6.2. Petrogenesis

The presence of inherited zircons suggests the involvement of a Neoarchean crust in the magma genesis of the Tongshi intrusive complex. The moderately high ε_{Nd} (t) and ε_{Hf} (t) values imply lithospheric mantle-derived materials participated in the formation of the quartz monzonites and the highest ε_{Nd} (t) and ε_{Hf} (t) values of the porphyritic syenites indicate involvement of asthenospheric mantle. We thus consider that crust–mantle interactions under different temperatures

Table 2
Sr–Nd–Pb isotopic compositions for the Tongshi intrusive complex and wallrocks.

Sample	Age (Ma)	Rb (ppm)	Sr (ppm)	$^{87}Rb/^{86}Sr$	$^{87}Sr/^{86}Sr$	±2σ	$(^{87}Sr/^{86}Sr)_i$	Sm (ppm)	Nd (ppm)	$^{147}Sm/^{144}Nd$	$^{143}Nd/^{144}Nd$	±2σ	$\varepsilon_{Nd}(t)$	$(^{206}Pb/^{204}Pb)i$	$(^{207}Pb/^{204}Pb)i$	$(^{208}Pb/^{204}Pb)i$
Fine-grained quartz monzodiorite																
08LX12	180	59.6	1213	0.1421	0.704099	9	0.703735	6.89	39.2	0.1064	0.511900	14	−12.3	15.964	15.035	35.693
08LX15	180	70.0	1166	0.1738	0.704258	17	0.703813	6.72	37.0	0.1099	0.511882	13	−12.8	16.184	15.122	35.997
08LX16	180	57.9	994	0.1686	0.704163	20	0.703731	5.71	32.5	0.1065	0.511900	11	−12.3	15.850	14.932	35.564
Porphyritic quartz monzodiorite																
08LX19	180	89.3	1328	0.1945	0.704174	15	0.703676	6.52	33.9	0.1166	0.512186	14	−7.0	16.721	15.113	36.337
08LX41	180	66.3	1408	0.1364	0.704200	19	0.703851	5.62	30.2	0.1126	0.511939	13	−11.7	16.452	15.184	36.212
08LX44	180	116	1406	0.2386	0.704759	15	0.704148	7.90	42.0	0.1139	0.512106	12	−8.5	16.881	15.261	36.562
Coarse-grained porphyritic syenite																
08LX21	180	243	698	1.0097	0.706269	9	0.703685	8.92	47.4	0.1140	0.512544	13	0.1	18.082	15.510	37.757
08LX37	180	421	372	3.2800	0.712162	15	0.703767	6.73	35.2	0.1157	0.512593	14	1.0	18.621	15.585	38.085
08LX39	180	953	353	7.8268	0.722394	12	0.702363	6.26	33.8	0.1122	0.512571	15	0.6	18.288	15.524	37.748
Medium-grained porphyritic syenite																
08LX25	180	372	908	1.1848	0.707914	12	0.704882	6.20	31.2	0.1203	0.512503	13	−0.9	19.560	15.730	39.498
08LX36	180	315	343	2.6634	0.710775	14	0.703959	3.88	20.2	0.1160	0.512617	35	1.5	18.555	15.564	38.222
Fine-grained porphyritic syenite																
08LX27	180	589	210	8.1358	0.728849	8	0.708028	1.92	16.7	0.0698	0.512439	12	−1.0	18.519	15.626	38.664
08LX34	180	794	101	22.7876	0.762374	13	0.704054	1.61	11.7	0.0835	0.512567	14	1.2	18.337	15.596	38.348
TTG gneiss																
07SD15	2500	104	599	0.5013	0.717938	9	0.699824	3.55	19.9	0.1078	0.511306	11	2.6	14.863	15.034	34.848

Chondrite Uniform Reservoir (CHUR) values ($^{87}Rb/^{86}Sr=0.0847$, $^{87}Sr/^{86}Sr=0.7045$, $^{147}Sm/^{144}Nd=0.1967$, $^{143}Nd/^{144}Nd=0.512638$) are used for the calculation. $\lambda_{Rb}=1.42\times10^{-11}$ year^{-1}, $\lambda_{Sm}=6.54\times10^{-12}$ year^{-1} (Lugmair and Harti, 1978). $\lambda_{U238}=1.55125\times10^{-10}$ year^{-1}, $\lambda_{U235}=9.8485\times10^{-10}$ year^{-1}, $\lambda_{Th232}=4.9475\times10^{-11}$ year^{-1} (Steiger and Jäger, 1977).

and depths were important for the generation of the Tongshi intrusive complex.

6.2.1. Quartz monzonites

AFC (assimilation and fractional crystallization) (DePaolo, 1981) and MASH (melting, assimilation, storage and homogenization) (Hildreth and Moorbath, 1988) are usually proposed to describe multiple and multistage magmatic processes. In the AFC model, crustal assimilation and fractional crystallization occur synchronously during magma ascent. In contrast, crustal melting and assimilation by primary magma as well as magma storage and homogenization proceed at the base of the crust in the MASH model. The homogeneous major and trace elements concentrations (Figs. 6 and 7) and Sr–Nd isotopic compositions (Fig. 8) within the fine-grained quartz monzonite suggest insignificant fractionation and crustal contamination during magma ascent, precluding AFC process in the magmatic evolution. Magma homogenization might have been achieved in the magma chamber and thus a process similar to MASH is envisaged for the fine-grained quartz monzonite. On the contrary, the negative correlations between TFe_2O_3 and SiO_2 (Fig. 11a), MgO and SiO_2 (Fig. 11b), CaO and SiO_2 (Fig. 11c) as well as between $\varepsilon_{Nd}(t)$ and SiO_2 (Fig. 11f) from the porphyritic quartz monzonite indicate that fractionation and crustal assimilation occurred during magma ascent, which is consistent with the AFC process.

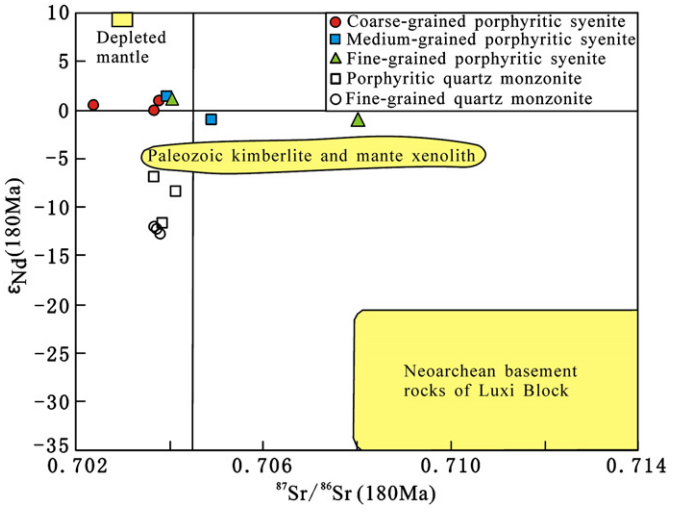

Fig. 8. Initial $^{87}Sr/^{86}Sr$ versus $\varepsilon_{Nd}(t)$ diagram for the Tongshi intrusive complex. Data for the Paleozoic kimberlite and mantle xenolith are from Yang et al. (2009) and Zhang et al. (2008). The field for Neoarchean basement rocks of Luxi Block is from Jahn et al. (1988) and Wang (2010). All $^{87}Sr/^{86}Sr$ and $\varepsilon_{Nd}(t)$ values are recalculated to 180 Ma.

Zircon saturation thermometry (T_{Zr}, Watson and Harrison, 1983) provides a simple and robust means of estimating magma temperatures from bulk-rock compositions. One of the important prerequisites for the application of zircon saturation thermometry is that zirconium is saturated in the melt. Based on a number of investigations, Miller et al. (2003) concluded that the presence of inherited zircon suggests saturation throughout the parent magma's history and T_{Zr} provides a useful estimate of initial magma temperature for plutons with abundant inherited zircons. Bulk-rock compositions and inherited zircons of the quartz monzonites match well with the requirements of using zircon saturation thermometry. Accordingly, the T_{Zr} calculated for the fine-grained quartz monzonite and the porphyritic quartz monzonite yield 746–762 °C (average 754 ± 5 °C) and 743–785 °C (average 759 ± 12 °C) respectively, which are taken to represent the initial magma temperatures of the quartz monzonites at the source. In order to verify the above temperature estimate, Ti-hornblende thermometer was also applied. Former studies have shown that Ti content of the hornblende increases strongly with temperature and Ti thermometer can be applied to magmatic hornblendes (Helz, 1973; Otten, 1984). The temperatures computed based on Ti-hornblende thermometer (Otten, 1984) are 746–782 °C (average 768 ± 13 °C) for the fine-grained quartz monzonite and

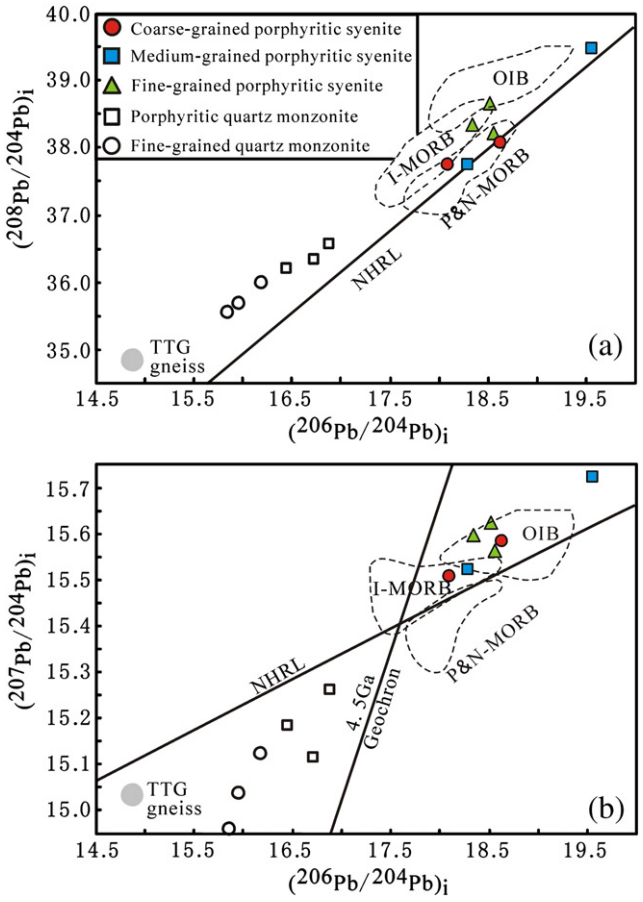

Fig. 9. $^{206}Pb/^{204}Pb$ vs. $^{208}Pb/^{204}Pb$ (a) and $^{206}Pb/^{204}Pb$ vs. $^{207}Pb/^{204}Pb$ (b) diagrams for the Tongshi intrusive complex.
The fields for I-MORB (Indian MORB), P&N-MORB (Pacific and North Atlantic MORB), OIB, NHRL and 4.55 Ga geochron are from Barry and Kent (1998), Hart (1984) and Zou et al. (2000).

749–781 °C (average 761 ± 14 °C) for the porphyritic quartz monzonite (Appendix Table S3). These values are consistent with those obtained from the zircon saturation thermometry. Experiments and modeling indicate that a water-rich fluid phase is required for inducing large-scale melting at $T<800$ °C within the crust (Miller et al., 2003). Since the breakdown of biotite and Ca-amphibole would not occur at $T<800$ °C (Miller et al., 2003), a model involving the dehydration melting of TTG gneisses is unrealistic to account for the quartz monzonites. Therefore, other sources enriched in fluids are required for inducing the melting. Basaltic injection into the crust has been widely considered as an important mechanism to generate silicic melts in the continental crust (Huppert and Sparks, 1988; Petford and Gallagher, 2001) and basalt can act either as a parental source or as the thermal trigger for crustal melting (Grunder, 1995; Xu et al., 2004). As indicated by the Nd and Hf isotopic compositions as well as the gabbroic enclaves, mantle-derived materials appear to have participated in the quartz monzonites and thus may have provided adequate fluids. Fluids would ascend into the zone of melting as a consequence of dehydration of hydrous mafic silicates in ultramafic–mafic rocks (Miller et al., 2003). The lithospheric mantle beneath Luxi Block, which was metasomatized by the subducted Yangtze slab during Mesozoic (Lan et al., 2011; Zhang et al., 2002, 2003, 2005), was enriched in fluids.

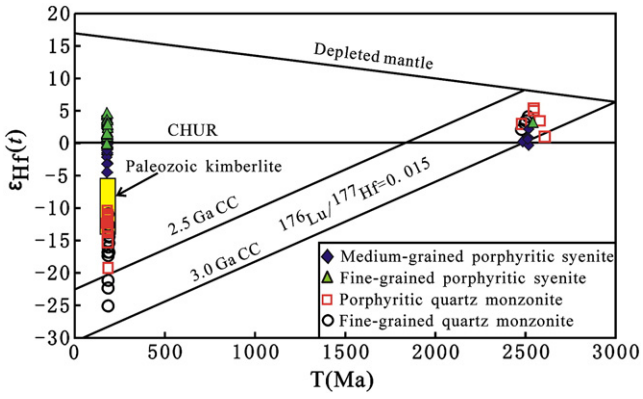

Fig. 10. Diagram of Hf isotopic evolution in zircons. CHUR, chondritic uniform reservoir; CC, continental crust. Depleted mantle evolution is calculated by using $\varepsilon_{Hf}(t) = 16.9$ at $t = 0$ Ma and $\varepsilon_{Hf}(t) = 6.4$ at $t = 3.0$ Ga. The corresponding lines of crustal extraction are calculated by using the $^{176}Lu/^{177}Hf$ ratio of 0.015 for the average continental crust (Griffin et al., 2002). Hf isotopic data for Paleozoic kimberlite are from Yang et al. (2009).

We thus envisage the following scenario for the origin of the Tongshi quartz monzonites. At about 185 Ma, partial melting of the Neoarchean crust, which was induced by the injection of lithospheric mantle-derived materials, produced the major melts of the fine-grained quartz monzonite. The crust-derived melts assimilated the mantle-derived materials and subsequently homogenized within the magma chamber, finally generating the fine-grained quartz monzonite through insignificant crustal contamination and fractionation. At about 182 Ma, as mafic melt injection continued, the crust-derived melt was mixed with more mantle-derived materials, forming the parental magma of the porphyritic quartz monzonite, which was emplaced at shallow crustal level after some crustal contamination and fractionation. Relative to the fine-grained quartz monzonite, the porphyritic quartz monzonite gained more mantle-derived materials (higher $\varepsilon_{Nd}(t)$ and $\varepsilon_{Hf}(t)$ values) and intruded in shallower crustal level (as suggested by the porphyritic texture), implying evolved crust–mantle interaction and continuous extension of the lithosphere from 185 Ma to 182 Ma.

6.2.2. Porphyritic syenites

The negative correlation between $\varepsilon_{Nd}(t)$ and SiO_2 within coarse-grained porphyritic syenite as well as within fine-grained porphyritic syenite (Fig. 11f) suggests that crustal contamination played a role during their formation. However, the lack of systematic variations in major elements (Fig. 11) within the individual porphyritic syenite plutons indicates that fractionation was probably insignificant in the magma evolution. This may be attributed to the fast cooling rate, as shown by their porphyritic texture. Therefore, a process different from AFC and MASH is proposed for the generation of the porphyritic syenites, which emphasizes crustal contamination instead of fractional crystallization. Considering the wide ranges of REE and trace elements concentrations (Fig. 7), the crustal materials involved probably originated from different depths varying from lower to upper crust. In summary, the formation of the porphyritic syenites was accomplished through partial melting of the asthenospheric mantle coupled with lower to upper crustal contamination.

6.3. Geodynamic significance

As a rare and isolated example for early Jurassic magmatism in the Luxi Block of eastern NCC, the geodynamic setting of the Tongshi intrusive complex has not been addressed in detail as yet. Apart from the Triassic continental collision (246–225 Ma) between NCC and YC (Liu and Xue, 2007; Zheng, 2008), there were no major geological events recognized around the Luxi Block during early Mesozoic. Therefore, the Triassic collision might have been the initial trigger for the early Jurassic magmatic activities and thus the Tongshi complex was probably generated in a post-collisional setting. Liégeois (1998) proposed three salient characteristics for post-collisional magmatism: (1) volumetrically the magmatic units are mainly

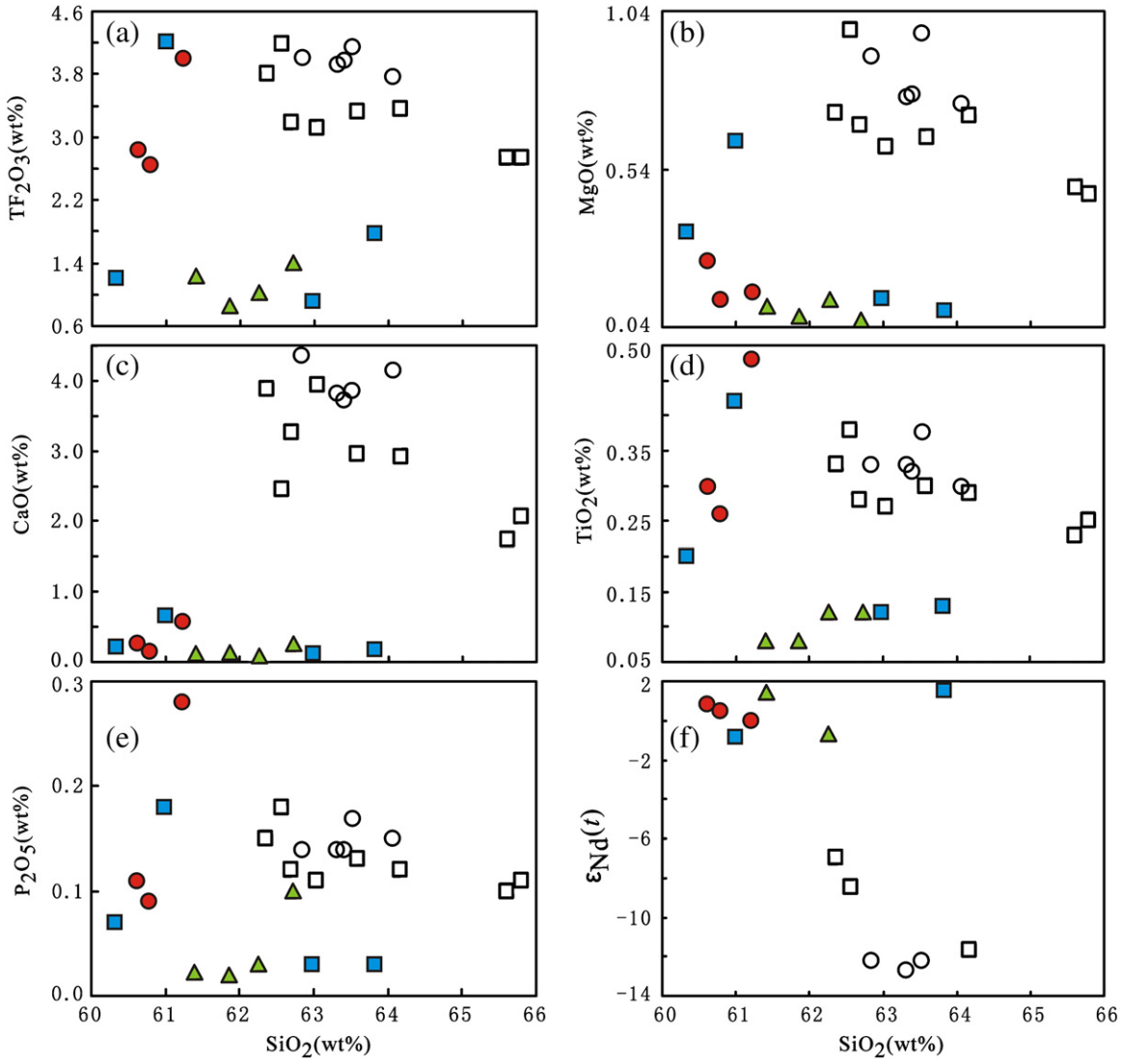

Fig. 11. Plots of TFe_2O_3 vs. SiO_2 (a), MgO vs. SiO_2 (b), CaO vs. SiO_2 (c), TiO_2 vs. SiO_2 (d), P_2O_5 vs. SiO_2 (e) and ε_{Nd} (t) vs. SiO_2 (f) for the Tongshi intrusive complex. Symbols are as in Fig. 9.

potassic and in particular high-K calc-alkaline with subordinate amount of shoshonitic rocks; (2) common linkage to large horizontal movements along major shear zones; (3) the source components were generated during the preceding subduction and collision period, whether it lies within the crust or lithospheric/asthenospheric mantle. The Tongshi intrusive complex confirms with most of the features for post-collisional magmatism as summarized below:

(1) High-K calc-alkaline (quartz monzonites) and shoshonitic series (porphyritic syenites) are present in the Tongshi intrusive complex, resembling rock associations developed during post-collisional period. The coeval occurrence of high-K calc-alkaline and shoshonitic series are typically observed in post-collisional settings (Bonin, 2004; Eyal et al., 2010; Liégeois et al., 1998; Litvinovsky et al., 2011; Miller et al., 1999; Seghedi and Downes, 2011), which are mainly attributed to the widespread K-rich sources produced in subduction zone. It is regarded that potassium metasomatism of the overlying lithospheric mantle is commonly generated by hybridization between slab-derived hydrous siliceous magmas and the overlying mantle wedge (Wyllie and Sekine, 1982; Zhang et al., 2010). The particularly fertile and fusible pockets of the volatile-enriched and K-rich mantle zones will preferably melt, giving rise to the high-K calc-alkaline series or even to shoshonitic series (Liégeois et al., 1998; Turner et al., 1996). In some cases, high-K calc-alkaline or shoshonitic rocks can also be produced by partial melting of asthenospheric mantle during post-collisional period due to slab breakoff or delamination of lithospheric mantle (Coulon et al., 2002; Eyal et al., 2010; Seghedi et al., 1998; Yang and Wu, 2009; Yang et al., 2007). Based on Nd and Hf isotopic compositions, we infer that the high K_2O contents of the quartz monzonites and porphyritic syenites from the Tongshi intrusive complex originated from lithospheric mantle and asthenospheric mantle respectively, which are consistent with high-K calc-alkaline and/or shoshonitic associations produced in post-collisional setting elsewhere.

(2) The emplacement of the Tongshi complex was controlled by the deep-rooted Tan–Lu Fault which was reactivated by the Triassic collision. Partial melting of asthenospheric mantle requires a lithosphere thinner than 80 km (McKenzie and Bickle, 1988; Xu et al., 2009), or needs deep lithospheric faults for decompression melting (Liégeois et al., 1998). Therefore, the asthenospheric mantle-derived porphyritic syenites of the Tongshi intrusive complex require that the lithosphere of the Luxi Block should have been thinner than 80 km or a deep-

rooted fault must been activated during early Jurassic. However, the Luxi Block had an ancient lithosphere thicker than 180 km prior to Mesozoic (Fan et al., 2000; Xu, 2001) and the lack of large-scale lithospheric mantle-derived as well as crust-derived magmas implies that significant lithospheric thinning might not have occurred during early Jurassic in the Luxi Block. The Tan–Lu Fault, which transected the continental crust to the crust–mantle boundary (Chen et al., 2008; Zhu et al., 2002), is located proximal to the Tongshi intrusive complex and was reactivated during 193–164 Ma (Wang et al., 2005; Zhu et al., 2004). Thus, a deep lithospheric fault might have been responsible for the emplacement of the porphyritic syenites (Fig. 12). The early Jurassic sinistral strike–slip movement of the Tan–Lu Fault (Wang et al., 2005) was consistent with large horizontal movements along major shear zones commonly developed in post-collisional settings (Liégeois, 1998; Liégeois et al., 1998).

(3) The complex sources of the Tongshi intrusion, which include ancient crust, enriched lithospheric mantle and asthenospheric mantle, are also similar to the diverse sources that are usually mobilized in post-collisional setting. The post-collisional period appears to be particularly efficient to mobilize different sources (Tack et al., 1994) mainly due to large-scale movements along mega-shear zones (Liégeois et al., 1998).

Several late Triassic intrusions (234–203 Ma), which are mainly distributed at the eastern margin of the NCC, have been correlated to the continental collision between NCC and YC and regarded to mark post-collisional magmatism (Peng et al., 2008; Seo et al., 2010; Williams et al., 2009; Yang and Wu, 2009; Yang et al., 2007). Geodynamic settings of these Triassic plutons remain controversial and various models including slab breakoff as well as delamination of lithospheric mantle have been proposed (Yang and Wu, 2009). However, regardless of the mechanism, the late Triassic magmatic pulses indicate that the eastern margin of the NCC was reactivated during the post-collisional process. The emplacement of the Tongshi intrusive complex postdated these late Triassic magmas by about 20–30 million years, probably implying the delayed effect of the post-collisional process towards the inner domain of the NCC (Fig. 12). A multi-source origin of the Tongshi complex suggests intense crust–mantle interaction and thus reactivation of the lithosphere in the inner part of the NCC must have been initiated from early Jurassic, which created the tectonic framework for significant lithospheric thinning and large-scale magmatism during early Cretaceous.

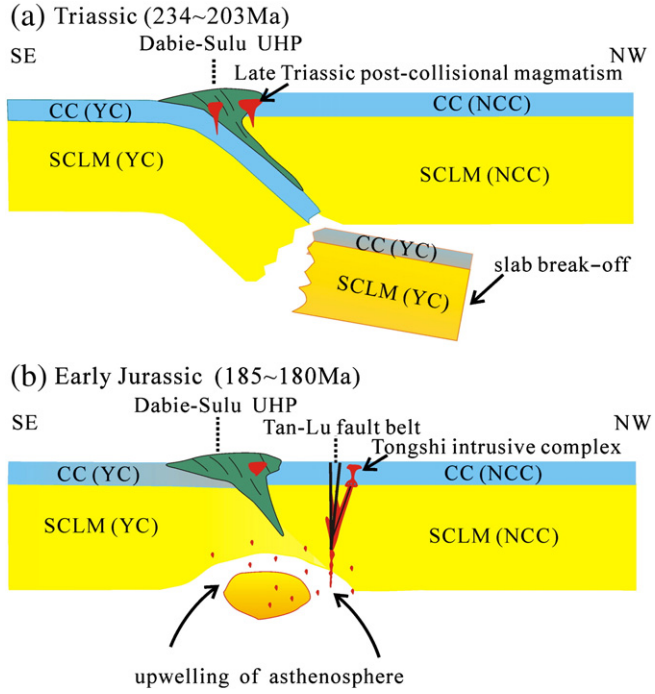

Fig. 12. Tectonic model for the generation of the Tongshi intrusive complex. (a) After early Triassic collision between NCC and YC, post-collisional magmatic activities were induced by slab break-off during late Triassic; (b) As post-collisional process going on, asthenospheric upwelling as well as activation of the deep-rooted Tan–Lu Fault triggered partial melting of the asthenospheric mantle, lithospheric mantle and ancient crust, generating the parental magmas of Tongshi intrusive complex in early Jurassic. SCLM, subcontinental lithospheric mantle; CC, continental crust; UHP, ultrahigh-pressure rocks; NCC, North China Craton; YC, Yangtze Craton. Late Triassic post-collisional magmatism was referenced to Chen et al. (2003), Peng et al. (2008), Yang et al. (2005, 2007) and Yang and Wu (2009).

7. Conclusions

1. The Tongshi intrusive complex is composed of quartz monzonites and porphyritic syenites, which can be classified into high-K calc-alkaline and shoshonitic series. The complex was emplaced during 180.1–184.7 Ma, and is a unique example for early Jurassic magmatism in Luxi Block of the eastern NCC.
2. The quartz monzonites of the Tongshi complex originated mainly through the partial melting of ancient crust coupled with the injection of enriched lithospheric mantle-derived materials, whereas the porphyritic syenites were derived largely from asthenospheric mantle with contamination of lower to upper crustal materials. Crust–mantle interaction to various degrees under different temperatures and depths was important for the generation of the Tongshi intrusive complex.
3. The rock associations and geochemical features of the Tongshi complex are consistent with post-collisional magmatism, suggesting their generation within post-collisional setting. The post-collisional magmatic process might have continuously modified the tectonic architecture of the NCC and finally contributed to the lithospheric destruction of this Craton.

Supplementary materials related to this article can be found online at doi:10.1016/j.lithos.2012.01.015.

Acknowledgments

We are grateful to Chao-Feng Li and Xiang-Hui Li for help during Sr, Nd and Pb isotope analyses and Zhao-Chu Hu for help during zircon LA–ICPMS U–Pb dating. Two anonymous reviewers and Editor-in-Chief Dr. Andrew Kerr are thanked for their constructive and valuable comments which greatly contributed to the improvement of the manuscript. This study was financially supported by the Natural Science Foundation of China (41172083 and 40625010), the Crisis Mines Continued Resources Exploration Project of China Geological Survey (20089930) and the China Postdoctoral Science Foundation (2011M500385).

References

Barry, T.L., Kent, R.W., 1998. Cenozoic magmatism in Mongolia and the origin of central and east Asian basalts. In: Flower, M.F.J., Chung, S.L., Lo, C.H., Lee, T.Y. (Eds.), Mantle Dynamics and Plate Interactions in East Asia. Geodynamics Series. American Geophysical Union, pp. 347–364.

Bonin, B., 2004. Do coeval mafic and felsic magmas in post-collisional to within-plate regimes necessarily imply two contrasting, mantle and crustal, sources? A review. Lithos 78, 1–24.

Chen, J.F., Xie, Z., Li, H.M., Zhang, X.D., Zhou, T.X., Park, Y.S., Ahn, K.S., Chen, D.G., Zhang, X., 2003. U–Pb zircon ages for a collision-related K-rich complex at Shidao in the Sulu ultrahigh pressure terrane, China. Geochemical Journal 37, 35–46.

Chen, L., Tao, W., Zhao, L., Zhen, T.Y., 2008. Distinct lateral variation of lithospheric thickness in the Northeastern North China Craton. Earth and Planetary Science Letters 267, 56–68.

Coulon, C., Megartsi, M., Fourcade, S., Maury, R.C., Bellon, H., Louni-Hacini, A., Cotton, J., Coutelle, A., Hermitte, D., 2002. Post-collisional transition from calc-alkaline to

alkaline volcanism during the Neogene in Oranie (Algeria): magmatic expression of a slab breakoff. Lithos 62, 87–110.
DePaolo, D.J., 1981. Trace element and isotopic effects of combined wallrock assimilation and fractional crystallization. Earth and Planetary Science Letters 53, 189–202.
Ernst, W.G., Tsujimori, T., Zhang, R., Liou, J.G., 2007. Permo-Triassic collision, subduction-zone metamorphism, and tectonic exhumation along the East Asian continental margin. Annual Review of Earth and Planetary Sciences 35, 73–110.
Eyal, M., Litvinovsky, B., Jahn, B.M., Zanvilevich, A., Katzir, Y., 2010. Origin and evolution of post-collisional magmatism: coeval Neoproterozoic calc-alkaline and alkaline suites of the Sinai Peninsula. Chemical Geology 269, 153–179.
Fan, W.M., Zhang, H.F., Baker, J., Jarvis, K.E., Mason, P.R.D., Menzies, M.A., 2000. On and off the North China Craton: where is the Archaean keel? Journal of Petrology 41, 933–950.
Galer, S.J.G., Abouchami, W., 1998. Practical application of lead triple spiking for correction of instrumental mass discrimination. Mineralogical Magazine 62A, 491–492.
Gao, S., Rudnick, R.L., Carlson, R.W., McDonough, W.F., Liu, Y.S., 2002. Re–Os evidence for replacement of ancient mantle lithosphere beneath the North China Craton. Earth and Planetary Science Letters 198, 307–322.
Gao, S., Zhang, J.F., Xu, W.L., Liu, Y.S., 2009. Delamination and destruction of the North China Craton. Chinese Science Bulletin 54, 3367–3378.
Geology and Mineral Resources Bureau of Shandong Province, 1995. Geological Map of Dongyang Area (1:50,000). Shandong Geological Printing House. (in Chinese).
Goolaerts, A., Mattielli, N., Jong, J.D., Weis, D., Scoatea, J.S., 2004. Hf and Lu isotopic reference values for the zircon standard 91500 by MC–ICP-MS. Chemical Geology 206, 1–9.
Griffin, W.L., Zhang, A.D., O'Reilly, S.Y., Ryan, C.G., 1998. Phanerozoic evolution of the lithosphere beneath the Sino–Korean Craton. In: Flower, M.F.J., Chung, S.L., Lo, C.H., Lee, T.Y. (Eds.), Mantle dynamics and plate interactions in East Asia: American Geophysical Union — Geodynamics Series, vol. 27, pp. 107–126.
Griffin, W.L., Wang, X., Jackson, S.E., Pearson, N.J., O'Reilly, S.Y., Xu, X.S., Zhou, X.M., 2002. Zircon chemistry and magma mixing, SE China: in-situ analysis of Hf isotopes, Tonglu and Pingtan igneous complexes. Lithos 61, 237–269.
Grunder, A.L., 1995. Material and thermal roles of basalt in crustal magmatism: case study from eastern Nevada. Geology 23, 952–956.
Hart, S.R., 1984. A large-scale isotope anomaly in the Southern Hemisphere mantle. Nature 309, 753–757.
Helz, R.T., 1973. Phase relations of basalts in their melting range at $P_{H2O} = 5$ kb as a function of oxygen fugacity. Part I. Mafic phases. Journal of Petrology 14, 249–302.
Hildreth, W., Moorbath, S., 1988. Crustal contributions to arc magmatism in the Andes of central Chile. Contributions to Mineralogy and Petrology 98, 455–489.
Huppert, H.E., Sparks, R.S.J., 1988. The generation of granitic magma by intrusion of basalt into continental crust. Journal of Petrology 29, 599–624.
Jahn, B.M., Auvray, B., Shen, Q.H., Liu, D.Y., Zhang, Z.Q., Dong, Y.J., Ye, X.J., Zhang, Q.Z., Cornichet, J., Mace, J., 1988. Archean crustal evolution in China: the Taishan complex, and evidence for juvenile crustal addition from long-term depleted mantle. Precambrian Research 38, 381–403.
Kusky, T.M., 2011. Geophysical and geological tests of tectonic models of the North China Craton. Gondwana Research 20, 26–35.
Lan, T.G., Fan, H.R., Hu, F.F., Tomkins, A.G., Yang, K.F., Liu, Y.S., 2011. Multiple crust–mantle interactions for the destruction of the North China Craton: geochemical and Sr–Nd–Pb–Hf isotopic evidence from the Longbaoshan alkaline complex. Lithos 122, 87–106.
Leake, B.E., Woolley, A.R., Arps, C.E.S., Birch, W.D., Gilbert, M.C., Grice, J.D., Hawthorne, F.C., Kato, A., Kisch, H.J., Krivovichev, V.G., Linthout, K., Laird, J., Mandarino, J.A., Maresch, W.V., Nickel, E.H., Rock, N.M.S., Schumacher, J.C., Smith, D.C., Stephenson, N.C.N., Ungaretti, L., Whittaker, E.J.W., Guo, Y., 1997. Nomenclature of amphiboles: report of the subcommittee on amphiboles of the International Mineralogical Association Commission on New Minerals and Mineral Names. The Canadian Mineralogist 35, 219–246.
Li, S.G., Xiao, Y.L., Liou, D.L., Chen, Y.Z., Ge, N.J., Zhang, Z.Q., Sun, S.S., Cong, B.L., Zhang, R.Y., Hart, S.R., Wang, S.S., 1993. Collision of the North China and Yangtze blocks and formation of coesite-bearing eclogites: timing and process. Chemical Geology 109, 89–111.
Liégeois, J.P., 1998. Preface — some words on the post-collisional magmatism. Lithos 45, 15–17.
Liégeois, J.P., Navez, J., Hertogen, J., Black, R., 1998. Contrasting origin of post-collisional high-K calc-alkaline and shoshonitic versus alkaline and peralkaline granitoids. The use of sliding normalization. Lithos 45, 1–28.
Litvinovsky, B.A., Tsygankov, A.A., Jahn, B.M., Katzira, Y., Be'eri-Shlevind, Y., 2011. Origin and evolution of overlapping calc-alkaline and alkaline magmas: the Late Palaeozoic post-collisional igneous province of Transbaikalia (Russia). Lithos 125, 845–874.
Liu, F.L., Xue, H.M., 2007. Review and prospect of SHRIMP U–Pb dating on zircons from Sulu–Dabie UHP metamorphic rocks. Acta Petrologica Sinica 23, 2737–2756 (in Chinese with English abstract).
Liu, Y.S., Hu, Z.C., Gao, S., Günther, D., Xu, J., Gao, C.G., Chen, H.H., 2008. In situ analysis of major and trace elements of anhydrous minerals by LA-ICP-MS without applying an internal standard. Chemical Geology 257, 34–43.
Liu, Y.S., Gao, S., Hu, Z.C., Gao, C.G., Zong, K., Wang, D., 2010. Continental and oceanic crust recycling-induced melt–peridotite interactions in the Trans-North China Orogen: U–Pb dating, Hf isotopes and trace elements in zircons of mantle xenoliths. Journal of Petrology 51, 537–571.
Ludwig, K.R., 2003. User's Manual for Isoplot 3.00, a geochronological Toolkit for Microsoft Excel. Berkeley Geochronological Center Special Publication, No. 4, pp. 25–32.
Lugmair, G.W., Harti, K., 1978. Lunar initial $^{143}Nd/^{144}Nd$: differential evolution of the lunar crust and mantle. Earth and Planetary Science Letters 39, 349–357.
McKenzie, D.P., Bickle, M.J., 1988. The volume and composition of melt generated by extension of the lithosphere. Journal of Petrology 29, 625–679.
Menzies, M.A., Xu, Y.G., 1998. Geodynamics of the North China Craton. In: Flower, M.F.J., Chung, S.L., Lo, C.H., Lee, T.Y. (Eds.), Mantle Dynamics and Plate Interactions in East Asia: American Geophysical Union — Geodynamics Series, vol. 27, pp. 155–165.
Middlemost, E.A.K., 1994. Naming materials in the magma/igneous rock system. Earth-Science Reviews 37, 215–224.
Miller, C., Schuster, R., Klötzli, U., Frank, W., Purtscheller, F., 1999. Post-collisional potassic and ultrapotassic magmatism in SW Tibet: geochemical and Sr–Nd–Pb–O isotopic constraints for mantle source characteristics and petrogenesis. Journal of Petrology 40, 1399–1424.
Miller, C.F., Mcdowell, S.M., Mapes, R.W., 2003. Hot and cold granites? Implications of zircon saturation temperatures and preservation of inheritance. Geology 31, 529–532.
Nehring, F., Foley, S.F., Höltta, P., Van den Kerkhof, A.M., 2009. Internal differentiation of the Archean continental crust: fluid-controlled partial melting of granulites and TTG-amphibolite associations in Central Finland. Journal of Petrology 50, 3–35.
Otten, M.T., 1984. The origin of brown hornblende in the Artfjallet gabbro and dolerites. Contributions to Mineralogy and Petrology 86, 189–199.
Patiño Douce, A.E., 1997. Generation of metaluminous A-type granites by low-pressure melting of calc-alkaline granitoids. Geology 25, 743–746.
Peccerillo, A., Taylor, S.R., 1976. Geochemistry of Eocene calc-alkaline volcanic rocks from the Kastamonu, northern Turkey. Contributions to Mineralogy and Petrology 58, 63–81.
Peng, P., Zhai, M.G., Guo, J.H., Zhang, H.F., Zhang, Y.B., 2008. Petrogenesis of Triassic post-collisional syenite plutons in the Sino–Korean craton: an example from North Korea. Geological Magazine 145, 637–647.
Petford, N., Gallagher, K., 2001. Partial melting of mafic (amphibolitic) lower crust by periodic influx of basaltic magma. Earth and Planetary Science Letters 193, 483–499.
Rapp, R.P., Watson, E.B., 1995. Dehydration melting of metabasalt at 8–32 kbar: implications for continental growth and crust–mantle recycling. Journal of Petrology 36, 891–931.
Santosh, M., 2010. Assembling North China Craton within the Columbia supercontinent: the role of double-sided subduction. Precambrian Research 178, 149–167.
Seghedi, I., Downes, H., 2011. Geochemistry and tectonic development of the Cenozoic magmatism in the Carpathian–Pannonian region. Gondwana Research 20, 655–672.
Seghedi, I., Balintoni, I., Szakács, A., 1998. Interplay of tectonics and Neogene post-collisional magmatism in the intracarpathian region. Lithos 45, 483–497.
Seo, J., Choi, S.G., Oh, C.W., 2010. Petrology, geochemistry, and geochronology of the post-collisional Triassic mangerite and syenite in the Gwangcheon area, Hongseong Belt, South Korea. Gondwana Research 18, 479–496.
Steiger, R.H., Jäger, E., 1977. Subcommission on geochronology: convention on the use of decay constants in geo- and cosmochronology. Earth and Planetary Science Letters 36, 359–362.
Sun, S.S., McDonough, W.F., 1989. Chemical and isotopic systematics of oceanic basalts: implications for mantle composition and processes. In: Saunders, A.D., Norry, M.J. (Eds.), Magmatism in the Oceanic Basalts: Geological Society Special Publication, pp. 313–345.
Tack, L., Liégeois, J.P., Deblond, A., Duchesne, J.C., 1994. Kibaran A-type granitoids and mafic rocks generated by two mantle sources in a late orogenic setting (Burundi). Precambrian Research 68, 323–356.
Turner, S., Arnaud, N., Liu, J., Rogers, N., Hawkesworth, C., Harris, N., Kelley, S., Van Calsteren, P., Deng, W., 1996. Post-collision, shoshonitic volcanism on the Tibetan plateau: implications for convective thinning of the lithosphere and the source of ocean island basalts. Journal of Petrology 37, 45–71.
Wang, W., 2010. The formation and evolution of granite–greenstone belt in the Qixingtai area, Western Shandong Province: constraints of geology, SHRIMP dating and geochemistry. Ph.D., dissertation, Chinese Academy of Geological Science, Beijing, pp. 1–119 (in Chinese with English abstract).
Wang, Y.S., Zhu, G., Chen, W., Song, C.Z., Liu, G.S., 2005. Thermochronologic information from the Tan–Lu Fault zone and its relationship with the exhumation of the Dabie Mountains. Geochimica 34, 193–214 (in Chinese with English abstract).
Watkins, J.M., Clemens, J.D., Treloar, P.J., 2007. Archaean TTGs as sources of younger granitic magmas: melting of sodic metatonalites at 0.6–1.2 GPa. Contributions to Mineralogy and Petrology 154, 91–110.
Watson, E.B., Harrison, T.M., 1983. Zircon saturation revisited: temperature and composition effects in a variety of crustal magma types. Earth and Planetary Science Letters 64, 295–304.
Williams, I.S., Cho, D.L., Kim, S.W., 2009. Geochronology, and geochemical and Nd–Sr isotopic characteristics, of Triassic plutonic rocks in the Gyeonggi Massif, South Korea: constraints on Triassic post-collisional magmatism. Lithos 107, 239–256.
Woodhead, J., Hergt, J., Shelley, M., Eggins, S., Kemp, R., 2004. Zircon Hf-isotope analysis with an excimer laser, depth profiling, ablation of complex geometries and concomitant age estimation. Chemical Geology 209, 121–135.
Wright, J.B., 1969. A simple alkalinity ratio and its application to questions of non-orogenic granite genesis. Geological Magazine 106, 370–384.
Wu, F.Y., Xu, Y.G., Gao, S., Zheng, J.P., 2008. Lithospheric thinning and destruction of the North China Craton. Acta Petrologica Sinica 24, 1145–1174 (in Chinese with English abstract).
Wyllie, P.J., Sekine, T., 1982. The formation of mantle phlogopite in subduction zone hybridization. Contributions to Mineralogy and Petrology 79, 375–380.
Xie, L.W., Zhang, Y.B., Sun, J.F., Wu, F.Y., 2008. In situ simultaneous determination of trace elements, U–Pb and Lu–Hf isotopes in zircon and baddeleyite. Chinese Science Bulletin 53, 1565–1573.

Xu, Y.G., 2001. Thermo-tectonic destruction of the Archean lithospheric keel beneath the Sino–Korean Craton: evidence, timing and mechanism. Physics and Chemistry of the Earth (Part A: Solid Earth and Geodesy) 26, 747–757.
Xu, Y.G., Huang, X.L., Ma, J.L., Wang, Y.B., Iizuka, Y., Xu, J.F., Wang, Q., Wu, X.Y., 2004. Crust–mantle interaction during the tectono-thermal reactivation of the North China Craton: constraints from SHRIMP zircon U–Pb chronology and geochemistry of Mesozoic plutons from western Shandong. Contributions to Mineralogy and Petrology 147, 750–767.
Xu, Y.G., Li, H.Y., Pang, C.J., He, B., 2009. On the timing and duration of the destruction of the North China Craton. Chinese Science Bulletin 54, 3379–3396.
Yang, J.H., Wu, F.Y., 2009. Triassic magmatism and its relation to decratonization in the eastern North China Craton. Science in China (Series D: Earth Sciences) 52, 1319–1330.
Yang, J.H., Chung, S.L., Wilde, S.A., Wu, F.Y., Chu, M.F., Lo, C.H., Fan, H.R., 2005. Petrogenesis of post-orogenic syenites in the Sulu Orogenic Belt, East China: geochronological, geochemical and Nd–Sr isotopic evidence. Chemical Geology 214, 99–125.
Yang, J.H., Wu, F.Y., Wilde, S.A., Liu, X.M., 2007. Petrogenesis of Late Triassic granitoids and their enclaves with implications for post-collisional lithospheric thinning of the Liaodong Peninsula, North China Craton. Chemical Geology 242, 155–175.
Yang, Y.H., Wu, F.Y., Wilde, S.A., Liu, X.M., Zhang, Y.B., Xie, L.W., Yang, J.H., 2009. In situ perovskite Sr–Nd isotopic constraints on the petrogenesis of the Ordovician Mengyin kimberlites in the North China Craton. Chemical Geology 264, 24–42.
Zhai, M.G., Santosh, M., 2011. The Early Precambrian odyssey of the North China Craton: a synoptic overview. Gondwana Research 20, 6–25.
Zhang, H.F., 2009. Peridotite–melt interaction: a key point for the destruction of cratonic lithospheric mantle. Chinese Science Bulletin 54, 3417–3437.
Zhang, H.F., Sun, M., Zhou, X.H., Fan, W.M., Zhai, M.G., Yin, J.F., 2002. Mesozoic lithosphere destruction beneath the North China Craton: evidence from major-, trace-element and Sr–Nd–Pb isotope studies of Fangcheng basalts. Contributions to Mineralogy and Petrology 144, 241–253.
Zhang, H.F., Sun, M., Zhou, X.H., Fan, W.M., Zheng, J.P., 2003. Secular evolution of the lithosphere beneath the eastern North China Craton: evidence from Mesozoic basalts and high-Mg andesites. Geochimica et Cosmochimica Acta 67, 4373–4387.
Zhang, H.F., Sun, M., Zhou, X.H., Ying, J.F., 2005. Geochemical constraints on the origin of Mesozoic alkaline intrusive complexes from the North China Craton and tectonic implications. Lithos 81, 297–317.
Zhang, X.M., Zhang, Y.Q., Ji, W., 2007. Fault distribution patterns of the Luxi Block, Shandong, and Mesozoic sedimentary–magmatic–structural evolution sequence. Journal of Geomechanics 13, 163–172 (in Chinese with English abstract).
Zhang, H.F., Goldstein, S.L., Zhou, X.H., Sun, M., Zheng, J.P., Cai, Y., 2008. Evolution of subcontinental lithospheric mantle beneath eastern China: Re–Os isotopic evidence from mantle xenoliths in Paleozoic kimberlites and Mesozoic basalts. Contributions to Mineralogy and Petrology 155, 271–293.
Zhang, S.B., Zheng, Y.F., Zhao, Z.F., Wu, Y.B., Yuan, H.L., Wu, F.Y., 2009. Origin of TTG-like rocks from anatexis of ancient lower crust: geochemical evidence from Neoproterozoic granitoids in South China. Lithos 113, 347–368.
Zhang, X.H., Zhang, H.F., Jiang, N., Zhai, M.G., Zhang, Y.B., 2010. Early Devonian alkaline intrusive complex from the northern North China craton: a petrological monitor of post-collisional tectonics. Journal of the Geological Society 167, 717–730.
Zhang, H.F., Yin, J.F., Tang, Y.J., Li, X.H., Feng, C., Santosh, M., 2011. Phanerozoic reactivation of the Archean North China Craton through episodic magmatism: evidence from zircon U–Pb geochronology and Hf isotopes from the Liadong Peninsula. Gondwana Research 19, 446–459.
Zhao, G.C., Wilde, S.A., Cawood, P.A., Sun, M., 2001. Archean blocks and their boundaries in the North China Craton: lithological, geochemical, structural and P–T path constraints and tectonic evolution. Precambrian Research 107, 45–73.
Zhao, G.C., Sun, M., Wilde, S.A., Li, S.Z., 2005. Late Archean to Paleoproterozoic evolution of the North China Craton: key issues revisited. Precambrian Research 136, 177–202.
Zheng, Y.F., 2008. A perspective view on ultrahigh-pressure metamorphism and continental collision in the Dabie–Sulu orogenic belt. Chinese Science Bulletin 53, 3081–3104.
Zheng, J.P., Griffin, W.L., O'Reilly, S.Y., Lu, F.X., Yu, C.M., Zhang, M., Li, H.M., 2004. U–Pb and Hf-isotope analysis of zircons in mafic xenoliths from Fuxian kimberlites: evolution of the lower crust beneath the North China Craton. Contributions to Mineralogy and Petrology 148, 79–103.
Zhu, G., Song, C.Z., Niu, M.L., Liu, G.S., Wang, Y.S., 2002. Lithospheric textures of the Tan–Lu Fault Zone and their genetic analysis. Geological Journal of China Universities 8, 248–256 (in Chinese with English abstract).
Zhu, G., Liu, G.S., Niu, M.L., Song, C.Z., Wang, D.X., 2003. Transcurrent movement and genesis of the Tan–Lu Fault Zone. Geological Bulletin of China 22, 200–207 (in Chinese with English abstract).
Zhu, G., Liu, G.S., Dunlap, W.J., Teyssier, C., Wang, Y.S., Niu, M.L., 2004. $^{40}Ar/^{39}Ar$ geochronological constraints on syn-orogenic strike–slip movement of Tan–Lu Fault Zone. Chinese Science Bulletin 49, 499–508.
Zou, H.B., Zindler, A., Xu, X.S., Qi, Q., 2000. Major, trace element, and Nd, Sr and Pb isotope studies of Cenozoic basalts in SE China: mantle sources, regional variations, and tectonic significance. Chemical Geology 171, 33–47.